Chronology of Episodic Accretion in Protostars—An ALMA Survey of the CO and H₂O Snowlines

Tien-Hao Hsieh[1] , Nadia M. Murillo[2], Arnaud Belloche[3] , Naomi Hirano[1] , Catherine Walsh[4] , Ewine F. van Dishoeck[2,5] ,
Jes K. Jørgensen[6] , and Shih-Ping Lai[1,7]

[1] Institute of Astronomy and Astrophysics, Academia Sinica, P.O. Box 23-141, Taipei 106, Taiwan; thhsieh@asiaa.sinica.edu.tw
[2] Leiden Observatory, Leiden University, P.O. Box 9513, 2300 RA, Leiden, The Netherlands
[3] Max-Planck-Institut für Radioastronomie, Auf dem Hügel 69, D-53121 Bonn, Germany
[4] School of Physics and Astronomy, University of Leeds, Leeds LS2 9JT, UK
[5] Max-Planck-Institut für extraterrestrische Physik, Giessenbachstraße 1, D-85748, Garching bei München, Germany
[6] Niels Bohr Institute, University of Copenhagen, Øster Voldgade 5–7, DK 1350 Copenhagen K., Denmark
[7] Institute of Astronomy, National Tsing Hua University (NTHU), Hsinchu 30013, Taiwan
Received 2019 July 4; revised 2019 September 5; accepted 2019 September 5; published 2019 October 21

Abstract

Episodic accretion has been used to explain the wide range of protostellar luminosities, but its origin and influence on the star-forming process are not yet fully understood. We present an ALMA survey of N_2H^+ $(1-0)$ and HCO^+ $(3-2)$ toward 39 Class 0 and Class I sources in the Perseus molecular cloud. N_2H^+ and HCO^+ are destroyed via gas-phase reactions with CO and H_2O, respectively, thus tracing the CO and H_2O snowline locations. A snowline location at a much larger radius than that expected from the current luminosity suggests that an accretion burst has occurred in the past that has shifted the snowline outward. We identified 18/18 Class 0 and 9/10 Class I post-burst sources from N_2H^+ and 7/17 Class 0 and 1/8 Class I post-burst sources from HCO^+. The accretion luminosities during the past bursts are found to be $\sim 10-100\,L_\odot$. This result can be interpreted as either evolution of burst frequency or disk evolution. In the former case, assuming that refreeze-out timescales are 1000 yr for H_2O and 10,000 yr for CO, we found that the intervals between bursts increase from 2400 yr in the Class 0 stage to 8000 yr in the Class I stage. This decrease in the burst frequency may reflect that fragmentation is more likely to occur at an earlier evolutionary stage when the young stellar object is more prone to instability.

Unified Astronomy Thesaurus concepts: Star formation (1569); Interstellar medium (847); Protostars (1302); Astrochemistry (75)

1. Introduction

Episodic accretion plays an important role in star formation (Audard et al. 2014). In the episodic accretion scenario, a protostellar system stays in a quiescent accretion phase most of the time, and accretion bursts occasionally occur to deliver material onto the central protostar. Because the accretion luminosity dominates the stellar luminosity at the early embedded phase (Hartmann & Kenyon 1996), this behavior leads to a low protostellar luminosity for the majority of the time. Such low luminosities have been revealed by recent surveys in star-forming regions with large statistical samples (Enoch et al. 2009; Evans et al. 2009; Kryukova et al. 2012; Hsieh & Lai 2013; Dunham et al. 2014), yet it is still unknown how the accretion luminosity evolves and affects the luminosity distribution (Offner & McKee 2011).

The origin of episodic accretion is still unknown owing to the difficulty in directly observing the accretion process. The most plausible explanation is disk instability, which can originate from several mechanisms such as thermal instability (Lin et al. 1985; Bell & Lin 1994), gravitational instability (Vorobyov & Basu 2005, 2010; Boley & Durisen 2008; Machida et al. 2011), and magnetorotational instability (Armitage et al. 2001; Zhu et al. 2009, 2010a, 2010b). Stellar (or planet) encounters have also been proposed to explain accretion bursts (Clarke & Syer 1996; Lodato & Clarke 2004; Forgan & Rice 2010). Furthermore, Padoan et al. (2014) suggest that the mass accretion rate is controlled by the mass infall from the large-scale turbulent cloud. These possibilities make episodic accretion a key mechanism in star formation because it is associated with

the timeline of disk fragmentation, planet formation, and multiplicity. Observationally, Liu et al. (2016) and Takami et al. (2018) found large-scale arms and arc structures in the disks toward four out of five FU Ori-type objects (Herbig 1966, 1977; see below) with $L_{bol} \sim 100-600\,L_\odot$. This supports the hypothesis that bursts are triggered by fragmentation due to gravitational instabilities. However, the remaining source, V1515 Cyg, hosts a smooth and symmetric disk. From an evolutionary point of view, Vorobyov & Basu (2015) find that the outburst should preferentially occur during the Class I stage after the disk has accreted sufficient material to fragment. However, Hsieh et al. (2018) found that accretion bursts with a few to a few tens of $L_\odot$ have occurred in very low luminosity objects (VeLLOs), which are extremely young or very low mass protostars and thus unlikely hosts of massive disks.

Episodic accretion alters the star formation process by regulating the radiative feedback (Offner et al. 2009). The change in the thermal structure of the disk can directly affect the chemical composition of gas and ice (Cieza et al. 2016; Wiebe et al. 2019). For example, Taquet et al. (2016) found that complex organic molecules could be formed via gas-phase reactions in the hot region ($T \gtrsim 100$ K) during the outburst phase. In a continuous accretion process, the radiative feedback could suppress fragmentation by keeping the disk and/or cloud core warm (Offner et al. 2009; Yıldız et al. 2012, 2015; Krumholz et al. 2014). On the contrary, episodic accretion can moderate this effect, and during the quiescent phase, the disk has sufficient time to cool down and fragment (Stamatellos et al. 2012). Such a process can be associated with the formation of

binary/multiple systems and the formation of substellar objects, affecting the multiplicity and initial mass function (Kratter et al. 2010; Stamatellos et al. 2011; Mercer & Stamatellos 2017; Riaz et al. 2018). Therefore, it is crucial to reveal the time intervals and the magnitude of outbursts in order to study how this radiative feedback affects the star formation process.

Variations in protostellar luminosity have been found in the past decades (i.e., FU Orionis and EX Orionis events; Herbig 1966, 1977), which are considered to arise directly from episodic accretion. Given the time intervals between bursts ($\sim 5 \times 10^3$–5×10^4 yr; Scholz et al. 2013), there are only a handful of cases in which luminosity variability has been reported to date (V1647 Ori, Ábrahám et al. 2004; Andrews et al. 2004; Acosta-Pulido et al. 2007; Fedele et al. 2007; Aspin et al. 2009; OO Serpentis, Kóspál et al. 2007; [CTF93]216-2, Caratti o Garatti et al. 2011; VSX J205126.1, Covey et al. 2011; Kóspál et al. 2011; HOPS 383, Safron et al. 2015). An outburst has also been detected toward the high-mass star-forming region S255IR-SMA1 (Caratti o Garatti et al. 2016; Liu et al. 2018). However, among these sources, HOPS 383 is the only source at an early stage (near the end of the Class I phase) owing to the difficulty of infrared/optical observations probing the embedded phase (Safron et al. 2015). At longer wavelengths, Liu et al. (2018) found variations in millimeter flux of 30%–60% toward 2 out of 29 sources using SMA. The James Clerk Maxwell Telescope (JCMT) transient survey monitored 237 sources at submillimeter wavelengths for 18 months (Herczeg et al. 2017; Johnstone et al. 2018), and they identified only one burst, from the Class I source EC53 (Yoo et al. 2007).

Chemical tracers are sensitive to the thermal history and can be used to probe past luminosity outbursts over a much longer timescale than direct observations of the luminosity (Lee 2007; Kim et al. 2011, 2012; Visser & Bergin 2012; Visser et al. 2015). Jørgensen et al. (2013) found a ring-like structure of $H^{13}CO^+$ surrounding the extended CH_3OH emission toward IRAS 15398 −3359. They found that this anticorrelation highlights the H_2O snowline location because CH_3OH has a sublimation temperature similar to that of H_2O and H_2O can destroy $H^{13}CO^+$ via gas-phase reactions (Visser et al. 2015). Given the current luminosity, they suggested that IRAS 15398−3359 has experienced a past luminosity outburst, sublimating H_2O over a larger region. This result was later confirmed with HDO by Bjerkeli et al. (2016), which directly revealed the radial extent of H_2O emission. Such an anticorrelation between H_2O and $H^{13}CO^+$ has also been found by van 't Hoff et al. (2018a) in NGC 1333 IRAS 2A, supporting that $H^{13}CO^+$ is a good tracer of the water snowline. An alternative method is to look directly at the CO snowline, which is at larger distances and can be more easily resolved using extended $C^{18}O$ emission. Jørgensen et al. (2015) and Frimann et al. (2017) studied 16 and 24 embedded protostars, respectively, and found that 20%–50% of the Class 0/I sources have experienced recent accretion bursts. Assuming a CO refreeze-out time of $\sim 10{,}000$ yr, they estimated that the time interval between accretion bursts is $(2$–$5) \times 10^4$ yr. Later, Hsieh et al. (2018) derived the CO snowline radius using the spatial anticorrelation of CO and N_2H^+ in VeLLOs and found that five out of seven sources are post-burst sources. On the other hand, using CO and N_2H^+ to trace the snowline, Anderl et al. (2016) found no evidence for past luminosity outbursts in four Class 0 protostars.

Here we present a survey of HCO^+ and N_2H^+, chemical tracers of past accretion bursts, in 39 protostars in Perseus, including 22 Class 0 sources and 17 Class I sources. In

Section 2 we describe the sample and the observations. The observational results are shown in Section 3, and the detailed analysis and the modeling are given in Section 4. Finally, we discuss the implications of our findings on episodic accretion and summarize these results in Sections 5 and 6, respectively.

2. Observations

2.1. Sample

We selected 39 protostars from Dunham et al. (2015) in Perseus ($d = 293$ pc; Ortiz-León et al. 2018), a star-forming region containing sufficient Class 0 and Class I sources for a statistical survey. These targets are located in the western Perseus region (Hsieh & Lai 2013) mostly near the NGC 1333 and B1 regions. Our sample includes 22 Class 0 and 17 Class I protostars with $T_{bol} = 25$–490 K (Table 1). The bolometric luminosities were taken from Dunham et al. (2015) and were scaled with the new measured distance (250 pc → 293 pc), which yields $L_{bol} = 0.1$–45 $L_{\odot}$. These 39 sources are selected because they are detected at 850 or 1120 μm continuum emission by single-dish observations (COMPLETE survey; Ridge et al. 2006); the presence of the continuum emission suggests that the envelope has not yet dissipated, which might be a marker of stronger line emission. All targets are included in the sample of the "Mass Assembly of Stellar Systems and their Evolution with the SMA (MASSES)" survey (Lee et al. 2015, 2016; Stephens et al. 2018), and we use the naming convention Per-emb-XX denoted by Enoch et al. (2009).

2.2. N_2H^+ (1−0) Observation

We observed the N_2H^+ (1−0) line emission toward 36 out of the 39 targets from 2018 March to 2018 April using ALMA (Cycle 5 project, 2017.1.01693.S, PI: T. Hsieh). The data is calibrated with ALMA pipeline using the CASA package version 5.1.1. The N_2H^+ (1−0) data for the remaining three targets are taken from an earlier ALMA project (2015.1.01576.S), the results of which were reported in Hsieh et al. (2018). With the C43-4 configuration, the resulting beam size was $\sim 2\rlap{.}''4 \times 1\rlap{.}''5$ using natural weighting. The largest scale covered is $\sim 12''$. The channel width was 30 kHz (~ 0.1 km s^{-1} at a frequency of 93 GHz). The on-source time toward each source was ~ 7.5 minutes, resulting in an rms noise level of ~ 13 mJy beam^{-1} at a spectral resolution of 0.1 km s^{-1}. The gain calibrator was J0336+3218 for all five executions. The flux and bandpass calibrators were J0237+2848 for three executions and J0238+1636 for the remaining two executions.

2.3. HCO^+ (3−2) and 1.2 mm Continuum Observations

The HCO^+ (3−2) data were taken simultaneously with the continuum and CH_3OH ($2_{0,2}$–$1_{-1,1}$) data toward the 39 targets in 2018 September during the same project (2017.1.01693.S). Data calibration was done by ALMA pipeline using the CASA package version 5.4. The integration time is ~ 12 minutes for each source. The array configuration was C43-5, resulting in a beam size of $0\rlap{.}''45 \times 0\rlap{.}''30$ using natural weighting and $0\rlap{.}''33 \times 0\rlap{.}''22$ using uniform weighting; for each source, we choose the weighting based on the signal-to-noise ratio of the image: uniform weighting is used for better-detected sources. The largest scale covered is $\sim 2\rlap{.}''6$. The channel widths for both HCO^+ and CH_3OH were 30.5 kHz (~ 0.03 km s^{-1}) and were averaged to 0.1 km s^{-1} when imaging. The rms noise level at a

Table 1
Targets

Source	Other Name	R.A. (J2000)	Decl. (J2000)	$F_{1.2\,mm}$ (mJy)	T_{bol} ($T_\odot$)	L_{bol} ($L_\odot$)	P.A. (deg)	Reference
Per-emb-2	IRAS 03292+3029	03^{h}32^{m}17^{s}92	+30^{d}49^{m}47^{s}85	702.0 ± 34.8	25	1.8	127	(1), (2), (3)
Per-emb-3		03^{h}29^{m}00^{s}58	+31^{d}12^{m}00^{s}17	52.6 ± 1.1	30	0.9	277	(1), (4)
Per-emb-4	DCE065	03^{h}28^{m}39^{s}11	+31^{d}06^{m}01^{s}66	0.9 ± 0.2	28	0.3	[a]50	(1), (5)
Per-emb-5	IRAS 03282+3035	03^{h}31^{m}20^{s}94	+30^{d}45^{m}30^{s}24	279.4 ± 4.5	32	1.6	125	(1), (2), (6)
Per-emb-6	DCE092	03^{h}33^{m}14^{s}41	+31^{d}07^{m}10^{s}69	10.7 ± 0.4	34	0.9	53	(1), (7)
Per-emb-7	DCE081	03^{h}30^{m}32^{s}70	+30^{d}26^{m}26^{s}47	8.1 ± 1.0	34	0.2	165	(1), (5)
Per-emb-9	IRAS 03267+3128, Perseus5	03^{h}29^{m}51^{s}83	+31^{d}39^{m}05^{s}85	11.1 ± 1.3	39	0.7	63	(1)
Per-emb-10		03^{h}33^{m}16^{s}43	+31^{d}06^{m}52^{s}01	21.9 ± 0.6	26	1.4	230	(1)
Per-emb-14	NGC 1333 IRAS 4C	03^{h}29^{m}13^{s}55	+31^{d}13^{m}58^{s}10	97.6 ± 1.7	35	1.2	95	(1), (8)
Per-emb-15	RNO15-FIR	03^{h}29^{m}04^{s}06	+31^{d}14^{m}46^{s}21	6.3 ± 0.9	17	0.9	145	(1), (4)
Per-emb-19	DCE078	03^{h}29^{m}23^{s}50	+31^{d}33^{m}29^{s}12	16.8 ± 0.4	60	0.5	335	(1), (7)
Per-emb-20	L1455-IRS4	03^{h}27^{m}43^{s}28	+30^{d}12^{m}28^{s}78	9.9 ± 1.5	54	2.3	295	(1)
Per-emb-22	L1448-IRS2	03^{h}25^{m}22^{s}41	+30^{d}45^{m}13^{s}21	51.4 ± 5.0	52	2.7	318	(1), (2), (8)
		03^{h}25^{m}22^{s}36	+30^{d}45^{m}13^{s}12	…	…	…	…	
Per-emb-24		03^{h}28^{m}45^{s}30	+31^{d}05^{m}41^{s}66	3.9 ± 0.3	62	0.6	281	(1), (8)
Per-emb-25		03^{h}26^{m}37^{s}51	+30^{d}15^{m}27^{s}79	120.5 ± 1.5	64	1.2	290	(1), (9), (10)
Per-emb-27	NGC 1333 IRAS 2A	03^{h}28^{m}55^{s}57	+31^{d}14^{m}36^{s}98	247.6 ± 12.4	54	30.2	204	(1), (2), (4)
		03^{h}28^{m}55^{s}57	+31^{d}14^{m}36^{s}42	…	…	…	…	
Per-emb-29	B1-c	03^{h}33^{m}17^{s}88	+31^{d}09^{m}31^{s}78	133.1 ± 5.5	41	4.8	110	(1)
Per-emb-30		03^{h}33^{m}27^{s}31	+31^{d}07^{m}10^{s}13	47.9 ± 0.8	62	1.8	109	(1), (11)
Per-emb-31	DCE064	03^{h}28^{m}32^{s}55	+31^{d}11^{m}05^{s}04	2.1 ± 0.4	52	0.4	345	(1), (7)
Per-emb-34		03^{h}30^{m}15^{s}17	+30^{d}23^{m}49^{s}19	11.4 ± 0.5	93	1.9	45	(1), (10)
Per-emb-35	NGC 1333 IRAS 1, Per-emb-35A	03^{h}28^{m}37^{s}09	+31^{d}13^{m}30^{s}76	27.8 ± 1.1	100	13.0	290	(1), (2), (6)
	Per-emb-35B	03^{h}28^{m}37^{s}22	+31^{d}13^{m}31^{s}73	…	…	…	…	
Per-emb-36	NGC 1333 IRAS 2B	03^{h}28^{m}57^{s}38	+31^{d}14^{m}15^{s}74	154.6 ± 3.0	100	7.3	204	(1), (2), (4)
Per-emb-38	DCE090	03^{h}32^{m}29^{s}20	+31^{d}02^{m}40^{s}75	26.0 ± 0.7	120	0.7	250	(1), (7)
Per-emb-39		03^{h}33^{m}13^{s}82	+31^{d}20^{m}05^{s}11	2.0 ± 0.4	59	0.1	…	(1)
Per-emb-40	B1-a	03^{h}33^{m}16^{s}67	+31^{d}07^{m}54^{s}87	16.9 ± 0.5	100	2.2	280	(1), (2)
Per-emb-41	B1b	03^{h}33^{m}20^{s}34	+31^{d}07^{m}21^{s}32	11.2 ± 0.4	47	0.8	210	(1), (6)
	B1b-S	03^{h}33^{m}21^{s}36	+31^{d}07^{m}26^{s}37	…	…	…	…	
Per-emb-44	SVS 13A, Per-emb-44-B	03^{h}29^{m}03^{s}75	+31^{d}16^{m}03^{s}77	313.6 ± 22.1	170	45.3	130	(1), (6)
	Per-emb-44-A	03^{h}29^{m}03^{s}77	+31^{d}16^{m}03.78 s	…	…	…	…	
	SVS 13A2	03^{h}29^{m}03^{s}39	+31^{d}16^{m}01^{s}58	…	…	…	…	
	SVS 13B	03^{h}29^{m}03^{s}08	+31^{d}15^{m}51^{s}70	…	…	…	…	
Per-emb-45		03^{h}33^{m}09^{s}58	+31^{d}05^{m}30^{s}94	1.4 ± 0.2	210	0.1	…	(1)
Per-emb-46		03^{h}28^{m}00.42 s	+30^{d}08^{m}00^{s}97	4.3 ± 0.4	230	0.3	315	(1)
Per-emb-48	L1455-FIR2	03^{h}27^{m}38^{s}28	+30^{d}13^{m}58^{s}52	4.0 ± 0.4	260	1.1	295	(1)
Per-emb-49	Per-emb-49-A	03^{h}29^{m}12.96 s	+31^{d}18^{m}14^{s}25	21.9 ± 1.9	240	1.4	207	(1), (6)
	Per-emb-49-B	03^{h}29^{m}12.98 s	+31^{d}18^{m}14.34 s	…	…	…	…	
Per-emb-51		03^{h}28^{m}34^{s}51	+31^{d}07^{m}05^{s}25	85.4 ± 4.3	150	0.2	110	(1)
Per-emb-52		03^{h}28^{m}39^{s}70	+31^{d}17^{m}31^{s}84	4.3 ± 0.4	250	0.2	25	(1)
Per-emb-54	NGC 1333 IRAS 6	03^{h}29^{m}01^{s}55	+31^{d}20^{m}20^{s}48	3.1 ± 0.4	230	11.3	310	(1)
Per-emb-58		03^{h}28^{m}58^{s}43	+31^{d}22^{m}17^{s}42	4.6 ± 0.2	240	1.3	5	(1)
Per-emb-59		03^{h}28^{m}35^{s}06	+30^{d}20^{m}09^{s}44	1.6 ± 0.1	49	0.5	…	(1)
Per-emb-63		03^{h}28^{m}43^{s}27	+31^{d}17^{m}32^{s}90	24.6 ± 0.5	490	2.2	[a]20	(1), 9
		03^{h}28^{m}43^{s}36	+31^{d}17^{m}32^{s}69	…	…	…	…	
		03^{h}28^{m}43^{s}57	+31^{d}17^{m}36^{s}31	…	…	…	…	
Per-emb-64		03^{h}33^{m}12^{s}85	+31^{d}21^{m}24^{s}00	39.7 ± 0.6	480	4.0	[a]70	(1)
Per-emb-65		03^{h}28^{m}56^{s}32	+31^{d}22^{m}27^{s}75	35.6 ± 0.7	440	0.2	140	(1)

Note. The source coordinates are obtained by a Gaussian fitting for the 1.2 mm images, and the fluxes are listed in the next column (Figure 1). The bolometric temperature (T_{bol}) and luminosity (L_{bol}) are taken from Dunham et al. (2015), in which L_{bol} is scaled to the new measured distance of Perseus (250 pc → 293 pc). We use $T_{bol} = 70$ K (Evans et al. 2009) as a boundary to classify Class 0 and Class I sources. The position angle (P.A.) of the outflow axis is taken from the corresponding references.

[a] The presumed P.A. of the source comes from disk or envelope structures rather than outflows.

References. (1) Stephens et al. 2018; (2) Tobin et al. 2016; (3) Schnee et al. 2012; (4) Plunkett et al. 2013; (5) Hsieh et al. 2018; (6) Lee et al. 2016; (7) Hsieh et al. 2017; (8) Tobin et al. 2015; (9) Segura-Cox et al. 2018; (10) Dunham et al. 2014; (11) Davis et al. 2008.

spectral resolution of 0.1 km s^{-1} is ~8–13 mJy beam^{-1} depending on the weighting. The window for continuum emission was centered at 268 GHz with a bandwidth of ~1.85 GHz. For all executions, the flux and bandpass calibrators were J0237+2848, and the phase calibrator was J0336+3218.

3. Results

3.1. Continuum Emission at 1.2 mm

Figure 1 shows the continuum emission at 1.2 mm of the sources in our sample. These maps are centered at the source
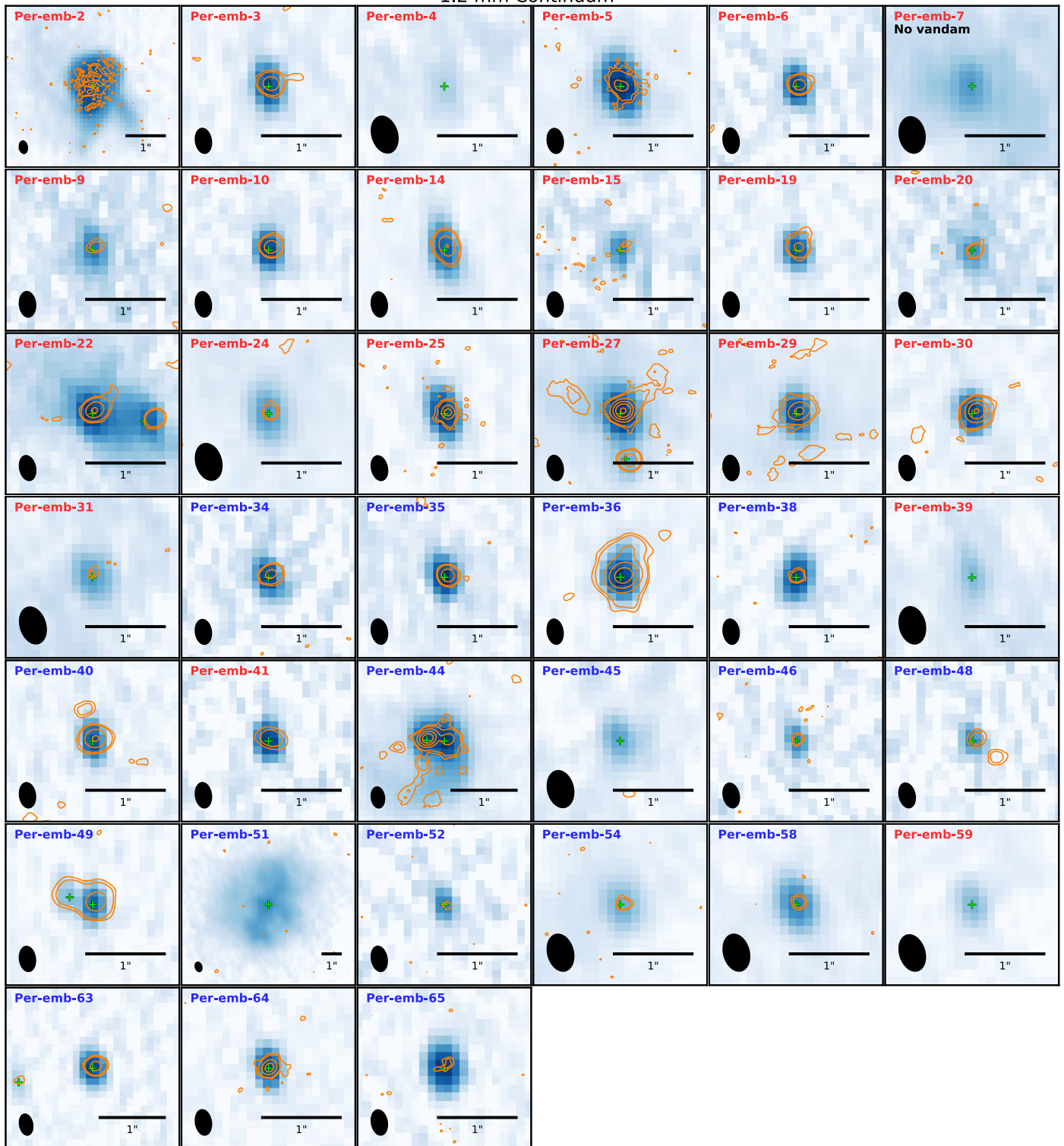
Figure 1. 1.2 mm dust continuum emission in color scale. The color scales are artificially adjusted with the fluxes of each source listed in Table 1. The orange contours show the 8 mm continuum emission with the contour levels of 3σ, 5σ, 20σ, 50σ, 100σ, 200σ from VANDAM (Tobin et al. 2016). The green cross indicates the position of the continuum emission from a Gaussian fitting. The source names are labeled in the upper left corner, and the color indicates the stages of the sources as Class 0 (red) or Class I (blue).

positions (as are the images in this paper) obtained from a Gaussian fitting to the continuum emission (Table 1). Table 1 lists also the Gaussian centers of the companion sources when detected. For these multiple systems, we use the coordinates

from the brightest sources at 1.2 mm as the system centers. The companions of Per-emb-40 and 48 found by the VLA Nascent Disk and Multiplicity Survey at 8 mm (Tobin et al. 2016) are not detected at 1.2 mm, probably due to insufficient sensitivity.
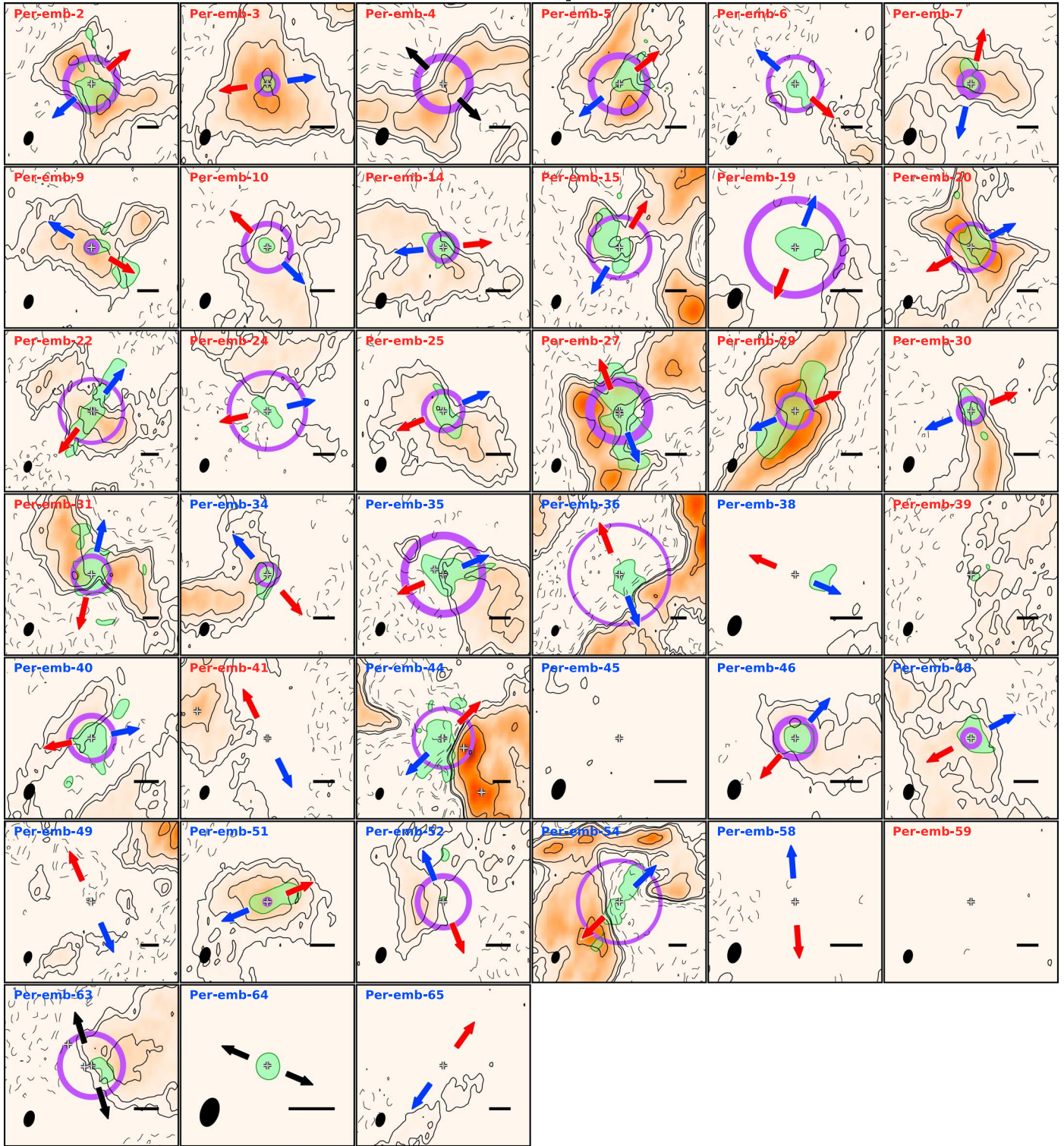
Figure 2. Integrated intensity maps of N_2H^+ (1−0) emission in orange scale and contours. The contour levels are 3σ, 5σ, 10σ, 20σ, and 40σ, with the rms noise level σ listed in Table 2. The green area shows the HCO^+ maps smoothed by a Gaussian kernel with $\sigma = 0\rlap{.}''5$ at a noise level of 3σ in order to compare with N_2H^+, and the original maps are shown in Figure 9. The black bar in the lower right corner indicates a size of $4''$, while the size of the image is adjusted panel by panel. The red and blue arrows show the outflow directions from the literature, and the black arrows denote the presumed outflow orientations from the disk or envelope structures. The white plus signs show the positions of the continuum sources (Table 1). The purple circles indicate the radii of the measured N_2H^+ peak, and their thicknesses represent the uncertainties (see the text for details).

3.2. N_2H^+ Maps

Figure 2 presents the N_2H^+ (1−0) integrated intensity maps, and the velocity ranges over which they were integrated are listed in Table 2. In order to maximize the signal-to-noise ratio, we integrated the emission from all seven hyperfine components in N_2H^+ (1−0). All targets are detected except for Per-emb-38, 45, 58, 59, and 64. For Per-emb-41, the N_2H^+ emission is likely associated with B1b-S located in the northeast. The N_2H^+

Table 2
N_2H^+ and HCO^+ Integrated Intensities

Source	N_2H^+			HCO^+		
	Beam (arcsec)	Vel. Range (km s^{-1})	rms (mJy beam^{-1} km s^{-1})	Beam (arcsec)	Vel. Range (km s^{-1})	rms (mJy beam^{-1} km s^{-1})
Per-emb-2	2.5 × 1.5	5.9–7.9	25.4	0.33 × 0.22	3.9–6.1, 7.9–9.3	10.0
Per-emb-3	2.5 × 1.5	6.2–8.0	24.1	0.33 × 0.22	5.1–6.4, 7.8–9.5	9.6
Per-emb-4	3.2 × 2.0	6.7–7.3	9.8	0.46 × 0.30	5.9–8.0	5.4
Per-emb-5	2.5 × 1.5	6.5–7.3	21.3	0.34 × 0.22	5.0–6.4, 8.2–9.5	9.1
Per-emb-6	2.5 × 1.5	5.6–6.2	16.3	0.43 × 0.29	5.1–5.4, 7.8–8.2	3.2
Per-emb-7	3.1 × 2.0	5.9–6.4	14.3	0.33 × 0.22	3.1–5.5, 6.6–8.4	10.8
Per-emb-9	2.5 × 1.5	7.7–8.3	17.8	0.34 × 0.22	5.0–7.6, 8.6–10.2	11.0
Per-emb-10	2.5 × 1.5	6.2–6.9	19.3	0.34 × 0.22	4.6–5.6, 7.4–8.7	8.4
Per-emb-14	2.5 × 1.5	6.5–8.7	25.3	0.34 × 0.22	5.0–6.7, 8.7–10.3	9.6
Per-emb-15	2.5 × 1.5	6.3–7.0	19.3	0.38 × 0.25	2.6–5.9, 8.7–9.0	7.8
Per-emb-19	2.5 × 1.5	7.2–7.7	18.5	0.38 × 0.25	6.0–6.9, 8.0–8.8	5.7
Per-emb-20	2.4 × 1.5	4.4–5.2	21.0	0.33 × 0.22	2.5–4.1, 6.2–8.3	10.6
Per-emb-22	2.4 × 1.5	3.5–4.7	23.0	0.33 × 0.22	1.2–3.3, 4.9–7.9	12.7
Per-emb-24	2.5 × 1.5	7.0–7.5	17.6	0.38 × 0.25	5.6–6.6, 8.1–9.1	6.1
Per-emb-25	2.3 × 1.5	4.7–5.6	20.8	0.33 × 0.22	2.7–4.6, 6.1–8.1	11.1
Per-emb-27	2.5 × 1.5	6.4–8.3	25.5	0.34 × 0.22	4.7–5.9, 8.8–10.8	9.6
Per-emb-29	2.5 × 1.5	5.4–7.2	24.4	0.34 × 0.22	3.9–5.7, 7.3–8.9	9.9
Per-emb-30	2.5 × 1.5	6.6–7.4	19.9	0.34 × 0.22	−0.1–6.1, 7.5–15.0	22.2
Per-emb-31	3.2 × 2.0	6.7–7.6	19.0	0.38 × 0.25	5.5–6.4, 7.9–9.4	7.0
Per-emb-34	2.4 × 1.5	5.6–6.4	21.3	0.33 × 0.22	1.6–5.1, 6.7–9.6	14.5
Per-emb-35	2.5 × 1.5	6.8–7.4	19.2	0.34 × 0.22	4.9–6.6, 8.0–9.6	10.5
Per-emb-36	2.5 × 1.5	7.0–7.6	18.3	0.34 × 0.22	1.1–5.8, 9.3–10.9	13.6
Per-emb-38	2.5 × 1.5	6.3–6.7	16.1	0.43 × 0.29	5.6–8.3	6.4
Per-emb-39	2.5 × 1.5	6.6–7.3	18.4	0.46 × 0.30	6.3–6.7	2.4
Per-emb-40	2.5 × 1.5	5.7–7.2	22.6	0.34 × 0.22	1.5–5.0, 7.8–11.5	14.8
Per-emb-41	2.5 × 1.5	6.4–6.9	17.4	0.46 × 0.30	5.8–7.6	5.2
Per-emb-44	2.5 × 1.5	7.7–9.1	23.3	0.34 × 0.22	6.6–8.3, 9.3–10.8	9.9
Per-emb-45	2.5 × 1.5	6.7–7.3	17.8	0.43 × 0.29	5.5–7.7	5.7
Per-emb-46	2.4 × 1.5	4.7–5.3	18.1	0.33 × 0.22	3.3–4.4, 5.3–5.8	7.0
Per-emb-48	2.4 × 1.5	3.9–5.2	22.1	0.43 × 0.28	1.2–3.5, 5.0–5.7	6.8
Per-emb-49	2.5 × 1.5	8.1–8.7	17.7	0.46 × 0.30	7.8–9.5	4.9
Per-emb-51	2.4 × 1.5	6.5–7.2	20.0	0.34 × 0.22	5.1–6.2, 7.1–7.9	7.7
Per-emb-52	2.5 × 1.5	7.6–8.2	18.1	0.46 × 0.30	6.9–7.7	3.4
Per-emb-54	2.5 × 1.5	7.7–8.4	19.5	0.38 × 0.25	3.0–7.6, 9.0–14.0	14.0
Per-emb-58	2.5 × 1.5	7.6–8.4	19.8	0.34 × 0.22	4.4–6.4, 9.1–10.5	10.4
Per-emb-59	2.4 × 1.5	5.2–5.8	18.7	0.45 × 0.30	5.6–7.6	5.7
Per-emb-63	2.5 × 1.5	7.5–8.3	19.7	0.38 × 0.25	6.9–8.6	5.6
Per-emb-64	2.5 × 1.5	4.1–4.6	17.5	0.34 × 0.22	−3.1–6.1, 7.7–15.0	26.2
Per-emb-65	2.5 × 1.5	8.4–9.2	21.0	0.46 × 0.30	6.5–9.1	6.2

emission in the Per-emb-39, 49, and 65 maps likely traces background cloud structures rather than the envelopes of the sources. These nondetected and ambiguous sources are thus excluded in the following analysis. As a result, 19 Class 0 and 11 Class I sources are remaining. In most of the sources, the N_2H^+ emission peaks are offset from the continuum source and are anticorrelated with HCO^+, which is also shown in Figure 2. This suggests that the N_2H^+ emission is suppressed in the warmer regions, where it is destroyed through reactions with CO sublimating off dust grains (Mauersberger & Henkel 1991; Jørgensen et al. 2004; van 't Hoff et al. 2017). Several targets show strong negative contours in the map, likely caused by the spatial filtering of large-scale emission. This is not expected to affect our analysis, in which we measure the peak position of the N_2H^+ emission and compare it with model predictions.

3.3. HCO+ Maps

The blow-ups of the HCO^+ integrated intensity maps are shown in Figure 9. We integrated the line emission excluding the optically thick region near the systemic velocity (Table 2; see Appendix A). This effect of optical depth is discussed in Section 4.4.1. The velocity ranges of integration are listed in Table 2. We removed the following sources in the analysis because the emission does not seem to reflect the H_2O snowline in the envelope: (1) Per-emb-4, 41, 49, and 59 show no detection near the source; (2) Per-emb-52 shows weak emission and ambiguous structures; and (3) for Per-emb-2, 36, 51, 64 and 65, the HCO^+ emission peaks near the outflows axes, which are likely associated with the outflows rather than the envelopes. We discuss if and how exclusion of these targets might introduce a bias. Most of these targets (except for Per-emb-4; see Section 4.1 and Hsieh et al. 2018) in categories (1) and (2) have no N_2H^+ detections, and in category (3), Per-emb-36, 64, and 65 also show no (or ambiguous) N_2H^+ detections. This suggests that their envelopes are almost dissipated; for Per-emb-36, 64, and 65 in category (3), outflows might dominate the emission with low envelope densities. Since the dissipation is likely associated with the evolution rather than one accretion outburst, we speculate that the removal of these
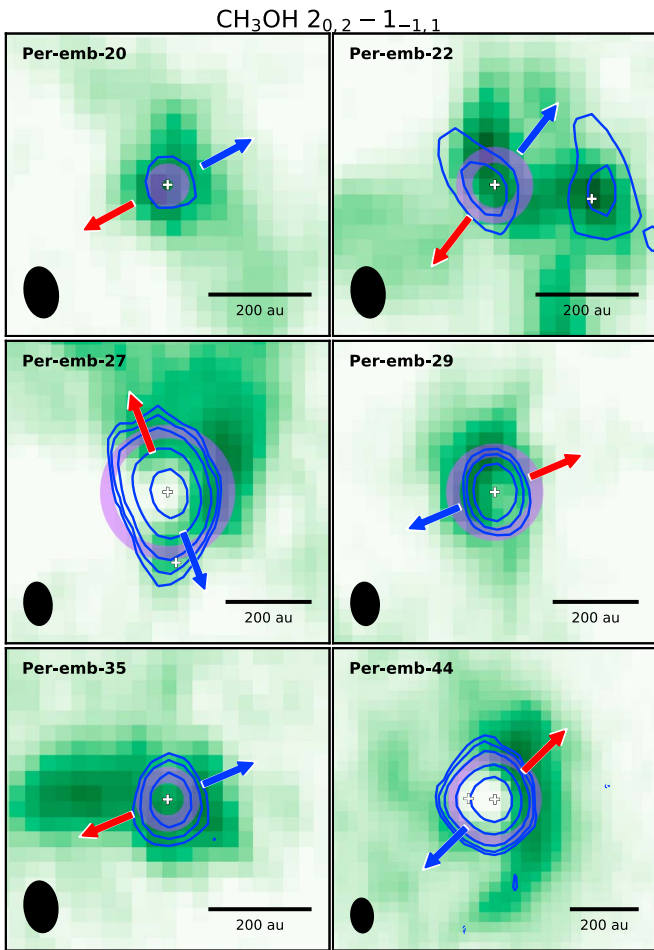
Figure 3. CH$_3$OH integrated intensity map (blue contours) overlaid on that of HCO$^+$ (green scale). The contour levels are 3σ, 5σ, 10σ, 30σ, and 70σ. The purple circles showing the radii of the measured HCO$^+$ peak are the same as described in Figure 9.

sources does not add a selection bias. However, this narrows down our sampling evolutionary phase in the more evolved Class I stage with $T_{bol} \gtrsim 250$ K. Per-emb-2 (Class 0) and Per-emb-51 (Class I) from category (3) can introduce a bias, but the small number only affects the statistical results by 5% for the Class 0 stage and by 11% for the Class I stage given the number of remaining sources. We note that in order to minimize the outflow contamination, our analysis focuses on the emission roughly along the axis perpendicular to the outflow. As a result, 18 Class 0 and 11 Class I sources are remaining for the following analysis.

3.4. CH$_3$OH ($2_{0,2}$–$1_{-1,1}$) Maps

CH$_3$OH ($2_{0,2}$–$1_{-1,1}$) at 254.015377 GHz is detected toward the source center in six targets (Figure 3). The emission most likely traces the region where CH$_3$OH sublimates owing to central heating. All these detected sources show an anticorrelation between CH$_3$OH and HCO$^+$ except for Per-emb-20 and 22, which have very weak CH$_3$OH emission. Because CH$_3$OH shares a similar sublimation temperature to H$_2$O ($\sim$100 K; Collings et al. 2004), these anticorrelations could be used to confirm the radii of the H$_2$O snowlines (van 't Hoff et al. 2018b). For Per-emb-20 and 22, CH$_3$OH emission and HCO$^+$ emission have a similar peak position at the center (see also Appendix C), which likely comes from unresolved

structures at the current resolution. However, the nondetections of CH$_3$OH do not indicate a temperature less than $\sim$100 K owing to the unknown CH$_3$OH abundance and probably the low Einstein coefficient of 1.9×10^{-5} s^{-1} for the transition. The origin and the presence or absence of CH$_3$OH emission will be discussed in a separate paper (N. M. Murillo et al. 2020, in preparation).

4. Analysis

In order to identify the post-burst sources, we model the line emission at different central luminosities. We compare the N$_2$H$^+$ and HCO$^+$ peak positions derived from the integrated intensity maps with those from the models. Here we describe how we measured the peak positions from the observed images (Section 4.1) and how we construct the models (Section 4.2). Then, we discuss the identification of sources that have likely experienced a past burst, i.e., post-burst sources, in Section 4.3, and we discuss the caveats in Section 4.4.

4.1. The Peak Radii in the Integrated Intensity Maps

The difficulty in measuring the radius of the emission peak is that the observed peak position is not always located at the equatorial plane, and such a plane is not necessarily perpendicular to the outflow. These misalignments can be reproduced by simulations (Offner et al. 2016) and are widely seen in observations (Hsieh et al. 2016; Lee et al. 2016; Stephens et al. 2018). To derive the radius of the peak emission, we employ a biconical mask to filter out the outflow-contaminated region; depending on sources, the region with a position angle smaller than 35°–85° from the outflow axis is excluded. We identify the local maxima from the resulting maps as the peak position of the emission on one or two sides. The mask in use and the selection of peak introduce artificial effects; taking the N$_2$H$^+$ emission in Per-emb-36 as an example, the measured radii of the emission peaks would be much smaller if the emission near the outflow axis were included in the analysis. Thus, we carefully check the integrated maps in each source. If only one peak is identified, the uncertainty is taken as the half-beam size. If two peaks are found, the peak radius is defined as the average of their distances to the primary source, and the uncertainty is taken as the difference of that but with a minimum value as the half-beam size (Figures 2, 9, and Table 3).

We check, using the images in Figure 2, whether the N$_2$H$^+$ peaks are located beyond the HCO$^+$-emitting region; HCO$^+$ is indeed expected to form from CO and traces the region where CO returns to the gas phase. We find that most of the HCO$^+$-emitting areas lie reasonably inside the N$_2$H$^+$ peak radii, at least along the major axis of the source. For several sources, the elongated HCO$^+$ emission is likely tracing the outflow and thus extends beyond the N$_2$H$^+$ peak radius (e.g., Per-emb-5, 7, 9, 22, 27, 29, 48, 51, and 54). This result suggests that the measured N$_2$H$^+$ peaks reflect the CO snowline radii. Per-emb-4 and 52 show N$_2$H$^+$ depletion without detections of HCO$^+$ toward the center. Per-emb-52 has extended C^{18}O emission toward the center (T. Hsieh 2020, in preparation). On the other hand, the CO isotopologues, ^{13}CO, C^{18}O, and C^{17}O (1−0) and (2−1) are not (or marginally) detected in Per-emb-4 (Hsieh et al. 2018; DCE065 in the paper). Thus, for Per-emb-4, we cannot exclude the possibility that N$_2$H$^+$ is absent owing

Table 3
Identification of the Past Burst from N_2H^+ and HCO^+

Name	L_{bol} ($L_\odot$)	$R_{N_2H^+peak}$ (arcsec)	$L_{burst,CO}$ ($L_\odot$)	$\dot{M}_{acc}$ ($10^{-6}\,M_\odot\,yr^{-1}$)	R_{HCO^+peak} (arcsec)	L_{burst,H_2O} ($L_\odot$)	$\dot{M}_{acc}$ ($10^{-6}\,M_\odot\,yr^{-1}$)	Last Burst (yr)
Per-emb-2	1.8	4.8 ± 0.9	$18.1^{+1.9}_{-0.1}$	$6.9^{+0.7}_{-0.1}$	...	...	...	<10,000
Per-emb-3	0.9	1.7 ± 0.9	$3.7^{+0.1}_{-0.3}$	$1.4^{+0.1}_{-0.1}$	0.16 ± 0.13	$1.6^{+1.1}_{-1.0}$	$0.6^{+0.4}_{-0.4}$	<1000
Per-emb-4	0.3	4.9 ± 1.3	$20.0^{+0.1}_{-1.9}$	$7.7^{+0.1}_{-0.7}$	...	...	...	[a]<10,000
Per-emb-5	1.6	5.2 ± 1.0	$22.1^{+0.1}_{-2.1}$	$8.5^{+0.1}_{-0.8}$	0.35 ± 0.14	$49.2^{+17.2}_{-22.2}$	$18.9^{+6.6}_{-8.5}$	<1000
Per-emb-6	0.9	5.0 ± 1.0	$20.0^{+0.1}_{-0.1}$	$7.7^{+0.1}_{-0.1}$	0.19 ± 0.18	$6.7^{+4.3}_{-5.7}$	$2.6^{+1.6}_{-2.2}$	<1000
Per-emb-7	0.2	2.0 ± 1.3	$4.5^{+0.1}_{-0.1}$	$1.7^{+0.1}_{-0.1}$	0.04 ± 0.13	<0.9	<0.3	1000–10,000
Per-emb-9	0.7	1.1 ± 1.0	$2.2^{+0.1}_{-0.2}$	$0.8^{+0.1}_{-0.1}$	0.06 ± 0.14	<0.9	<0.3	1000–10,000
Per-emb-10	1.4	3.8 ± 1.0	$12.1^{+1.3}_{-0.1}$	$4.6^{+0.5}_{-0.1}$	0.10 ± 0.14	<0.9	<0.3	1000–10,000
Per-emb-14	1.2	2.2 ± 1.0	$4.9^{+0.1}_{-0.1}$	$1.9^{+0.1}_{-0.1}$	0.31 ± 0.14	$40.3^{+14.1}_{-22.2}$	$15.4^{+5.4}_{-8.5}$	<1000
Per-emb-15	0.9	5.7 ± 0.9	$24.4^{+0.1}_{-0.1}$	$9.4^{+0.1}_{-0.1}$	0.03 ± 0.15	<1.6	<0.6	1000–10,000
Per-emb-19	0.5	5.9 ± 1.0	$27.0^{+0.1}_{-0.1}$	$10.4^{+0.1}_{-0.1}$	0.14 ± 0.16	<1.8	<0.7	1000–10,000
Per-emb-20	2.3	4.4 ± 0.9	$16.4^{+0.1}_{-1.6}$	$6.3^{+0.1}_{-0.6}$	0.09 ± 0.14	<0.9	<0.3	1000–10,000
Per-emb-22	2.7	7.1 ± 0.9	$36.4^{+0.1}_{-0.1}$	$14.0^{+0.1}_{-0.1}$	0.20 ± 0.14	$8.1^{+6.7}_{-6.9}$	$3.1^{+2.6}_{-2.6}$	<1000
Per-emb-24	0.6	7.1 ± 0.9	$36.4^{+0.1}_{-0.1}$	$14.0^{+0.1}_{-0.1}$	0.26 ± 0.15	$24.4^{+12.0}_{-19.5}$	$9.4^{+4.6}_{-7.5}$	<1000
Per-emb-25	1.2	3.1 ± 0.9	$9.0^{+0.1}_{-0.9}$	$3.5^{+0.1}_{-0.3}$	0.29 ± 0.13	$36.4^{+12.8}_{-24.3}$	$14.0^{+4.9}_{-9.3}$	<1000
Per-emb-27	30.2	5.5 ± 1.0	$24.4^{+0.1}_{-2.3}$	$9.4^{+0.1}_{-0.9}$	0.48 ± 0.14	$99.1^{+0.1}_{-25.7}$	$38.0^{+0.1}_{-9.9}$	0
Per-emb-29	4.8	3.1 ± 1.0	$9.0^{+0.1}_{-0.9}$	$3.5^{+0.1}_{-0.3}$	0.33 ± 0.14	$44.5^{+15.6}_{-22.4}$	$17.1^{+6.0}_{-8.6}$	<1000
Per-emb-30	1.8	2.0 ± 1.0	$4.5^{+0.1}_{-0.4}$	$1.7^{+0.1}_{-0.2}$	0.13 ± 0.14	<0.9	<0.3	1000–10,000
Per-emb-31	0.4	4.6 ± 1.3	$18.1^{+0.1}_{-1.7}$	$6.9^{+0.1}_{-0.7}$	0.34 ± 0.15	$49.2^{+17.2}_{-24.8}$	$18.9^{+6.6}_{-9.5}$	<1000
Per-emb-34	1.9	2.0 ± 0.9	$4.0^{+0.4}_{-0.1}$	$1.5^{+0.2}_{-0.1}$	0.18 ± 0.14	$5.4^{+2.7}_{-4.5}$	$2.1^{+1.0}_{-1.7}$	<1000
Per-emb-35	13.0	7.3 ± 0.9	$40.3^{+0.1}_{-0.1}$	$15.4^{+0.1}_{-0.1}$	0.16 ± 0.14	$1.6^{+1.1}_{-1.0}$	$0.6^{+0.4}_{-0.4}$	1000–10,000
Per-emb-36	7.3	12.4 ± 0.9	$109.5^{+0.1}_{-0.1}$	$42.0^{+0.1}_{-0.1}$	...	...	...	<10,000
Per-emb-38	0.7	...	...	...	0.05 ± 0.18	<6.7	<2.6	>1000
Per-emb-39	0.1	...	...	...	0.23 ± 0.19	$13.4^{+11.0}_{-11.6}$	$5.1^{+4.2}_{-4.4}$	<1000
Per-emb-40	2.2	3.6 ± 1.0	$11.0^{+1.2}_{-0.1}$	$4.2^{+0.5}_{-0.1}$	0.08 ± 0.14	<0.9	<0.3	1000–10,000
Per-emb-41	0.8	...	...	...	...	...	...	...
Per-emb-44	45.3	6.6 ± 1.0	$33.0^{+0.1}_{-0.1}$	$12.7^{+0.1}_{-0.1}$	0.41 ± 0.14	$73.4^{+7.7}_{-24.2}$	$28.1^{+3.0}_{-9.3}$	0
Per-emb-45	0.1	...	...	...	0.07 ± 0.18	<6.7	<2.6	>1000
Per-emb-46	0.3	2.4 ± 0.9	$5.4^{+0.1}_{-0.1}$	$2.1^{+0.1}_{-0.1}$	0.12 ± 0.13	<0.9	<0.3	1000–10,000
Per-emb-48	1.1	1.3 ± 0.9	$2.7^{+0.3}_{-0.3}$	$1.0^{+0.1}_{-0.1}$	0.39 ± 0.17	$66.4^{+14.7}_{-26.1}$	$25.5^{+5.6}_{-10.0}$	<1000
Per-emb-49	1.4	...	...	...	...	...	...	...
Per-emb-51	0.2	0.3 ± 1.0	<2.2	<0.8	...	...	...	>10,000
Per-emb-52	0.2	4.2 ± 0.9	$14.8^{+0.1}_{-1.4}$	$5.7^{+0.1}_{-0.5}$	...	...	...	<10,000
Per-emb-54	11.3	9.2 ± 0.9	$60.1^{+6.3}_{-0.1}$	$23.0^{+2.4}_{-0.1}$	0.11 ± 0.15	<1.6	<0.6	1000–10,000
Per-emb-58	1.3	...	...	...	0.05 ± 0.14	<0.9	<0.3	>1000
Per-emb-59	0.5	...	...	...	...	...	...	...
Per-emb-63	2.2	5.1 ± 0.9	$20.0^{+2.1}_{-0.1}$	$7.7^{+0.8}_{-0.1}$	0.15 ± 0.15	<1.6	<0.6	1000–10,000
Per-emb-64	4.0	...	...	...	...	...	...	...
Per-emb-65	0.2	...	...	...	...	...	...	...

Note. Column (1): source name. Column (2): bolometric luminosity from Dunham et al. (2014) scaled from 230 to 293 pc. Column (3): radius of the measured N_2H^+ peak. Column (4): luminosity corresponding to the radius of the measured N_2H^+ peak from models, i.e., the accretion luminosity during the past burst. Column (5): mass accretion rate estimated from Column (4). Columns (6)–(8): same as Columns (3)–(5), but with the numbers measured from HCO^+. Column (9): rime after the last burst.
[a] Per-emb-4 has no HCO^+ and CO detection toward the center. Thus, it is unclear whether the N_2H^+ depletion comes from destruction by CO or freeze-out of the parent molecule, N_2.

to freeze-out of N_2 in the central dense region (Belloche & André 2004).

We check whether the HCO^+ peaks are located beyond the CH_3OH-emitting regions for the six sources with CH_3OH detections (Figure 3). The spatial extent of CH_3OH emission is broadly within the radius of the measured HCO^+ peak. This suggests that HCO^+ reflects well the H_2O sublimation region and that the measured radii are reasonable. Unfortunately, most of the sources have no CH_3OH detection; such nondetections do not rule out the hypothesis that HCO^+ probes the location of the H_2O snowline but prevent us from confirming it.

Figure 4 shows the intensity profiles of N_2H^+, HCO^+, and CH_3OH toward four standard sources along cuts across the source center and the identified local maxima. Anticorrelations are clearly seen in all plots except for N_2H^+-HCO^+ in Per-emb-51 and HCO^+-CH_3OH in Per-emb-20. In the latter two cases, although these intensity profiles share a similar peak position, the HCO^+ emission in Per-emb-51 and CH_3OH emission in Per-emb-20 are both very weak. The common peaks most likely come from an unresolved region smaller than the beam. The intensity profiles for all targets are shown in Appendix C.
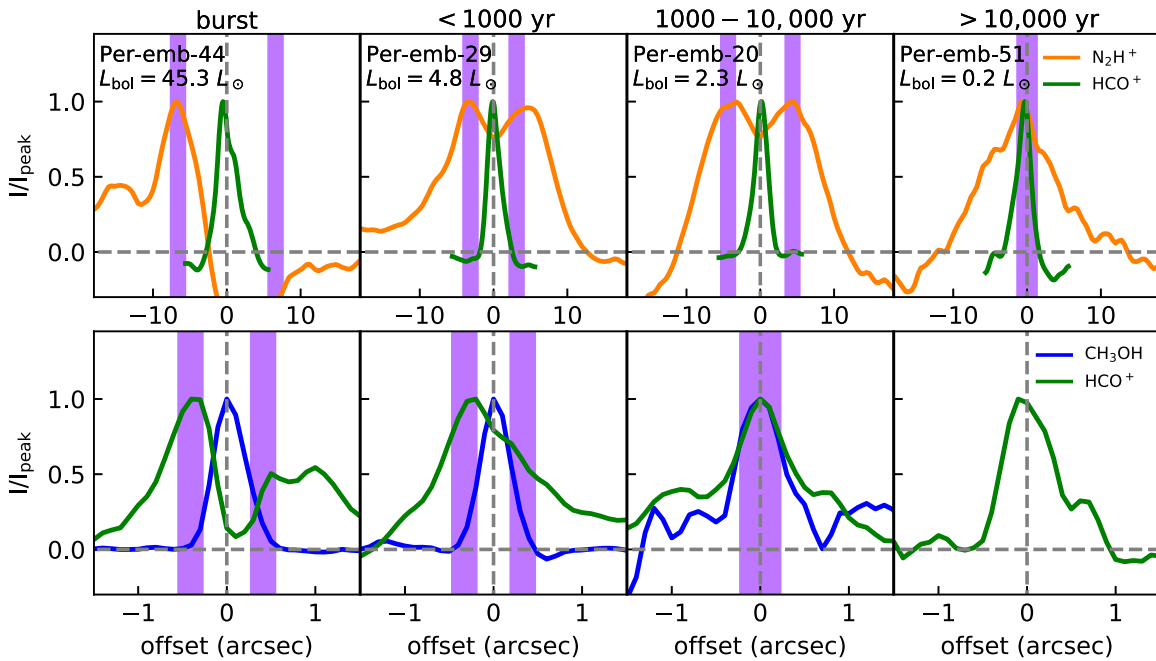
Figure 4. Intensity profiles along cuts across the source center and the local minima from the integrated intensity maps toward four sources. The top panel shows the N_2H^+ and smoothed HCO^+ profiles at large scales, and the bottom panel shows the HCO^+ and CH_3OH profiles at small scales. The profiles are normalized to their peaks. The bolometric luminosity of the target is labeled in the upper left corner. The purple area indicates the radius of the measured peak for N_2H^+ (top) and HCO^+ (bottom) in Table 3. The vertical and horizontal dashed lines represent the source position and the intensity zero level, respectively.

4.2. MHW20 Models

To help the interpretation of the observational data, we construct a model framework for studying the relation between the luminosity and the emission peak radii of N_2H^+ and HCO^+ (N. M. N. M. Murillo 2020, in preparation, hereafter MHW20). MHW20 have built a grid of density structures by varying the disk and envelope geometry. For each density structure, RADMC3D[8] (Dullemond et al. 2012) is employed to calculate the temperature profile with a given central luminosity from 0.01 to 200 $L_\odot$. These physical conditions are later used for deriving the molecular abundance profiles. The model starts from initially icy H_2O and CO, and a chemical network based on the UMIST database for Astrochemistry, version RATE12 (McElroy et al. 2013), is used to calculate the static chemical abundance profiles. The abundances of CO, N_2, and H_2O relative to H_2 are set to 2×10^{-4}, 1×10^{-4}, and 2×10^{-4}, respectively. A constant cosmic-ray ionization rate appropriate for the interstellar medium, 1.2×10^{-17} s^{-1}, is adopted. It is noteworthy that Padovani et al. (2016) found that the shocked gas from protostellar jets enhances the ionization rate by a few orders of magnitude, which can affect the abundances of HCO^+ and N_2H^+ (Gaches et al. 2019). However, this effect is less significant in the midplane of a flattened envelope, which is the region in which we are interested.

Due to central heating, CO and H_2O are sublimated from the dust grains and destroy N_2H^+ and HCO^+ via the gas-phase reactions

$$CO + N_2H^+ \longrightarrow HCO^+ + N_2$$

and

$$H_2O + HCO^+ \longrightarrow H_3O^+ + CO,$$

respectively (see Section 1). Thus, N_2H^+ and HCO^+ are expected to be depleted in the central regions, where the temperature is higher than the sublimation temperatures of CO ($\sim$20 K) and H_2O ($\sim$100 K), respectively. Finally, MHW20 make emission-line images using the line radiative transfer code available as part of RADMC3D using molecular transition data from the Leiden database (Schöier et al. 2005) (N_2H^+ from Green 1975 and HCO^+ from Flower 1999). These images perform as a reference for comparison with observations with different burst luminosities L_{burst}.

In this work, we adopt the model with a rotationally flattened envelope given by Ulrich (1976), i.e., without a disk component, from MHW20. We include an outflow cavity with the edge, $z(r)$, following the function $z(r) \propto r^{1.5}$ with an opening angle of 50° at $z = 50$ au (Whitney et al. 2003; Robitaille et al. 2006). For a quantitative comparison between the model and observation, we measure the molecular peak radii from the models with different luminosities at different inclination angles (see Appendix B). Here we show an example comparing the observed N_2H^+ and HCO^+ integrated intensity maps of Per-emb-5 to that of the model (Figure 5); the modeled image is generated using the CASA task "simobserve" for a source with a luminosity of 30 $L_\odot$ at an inclination angle of 45°. Figure 6 compares the modeled and observed molecular peak radii as a function of luminosity. The modeled peak radius is affected by the inclination owing to the emission contributed from the inner or outer envelope (see Appendix B). Besides, because a disk could shield the outer region from the central radiative heating, the modeled luminosity should be considered as a lower limit; if a disk exists, a higher luminosity is needed to shift the peak position outward to match the observation (see the disk model in Figure 6).

---

[8] http://www.ita.uni-heidelberg.de/~dullemond/software/radmc-3d/
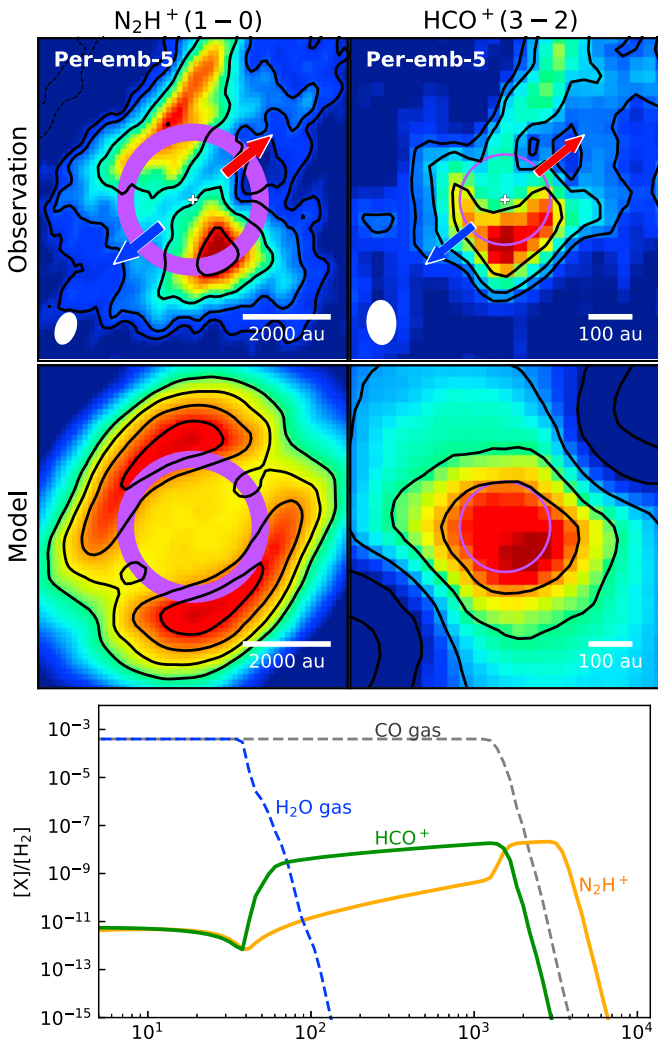
Figure 5. Example showing the comparison of the observations and models for Per-emb-5. The top row shows the observed N_2H^+ map (left) and HCO^+ map (right) in the same contours as in Figures 2 and 9. These images are at different sizes, with scale bars shown in the bottom right corner. The images of a model with 30 $L_\odot$ are shown in the second row, with arbitrary intensity scales and contours to emphasize the emission peak. The purple circles indicate the radii of the N_2H^+ and HCO^+ peaks in the corresponding map from observations. The bottom panel shows the molecular abundance profiles in the equatorial plane for the model.

4.3. Identification of Post-burst Sources

Figure 6 shows the measured radii of N_2H^+ and HCO^+ emission peaks as a function of the source bolometric luminosity. If the observed peak radius is larger than the predicted value from the model at the given luminosity, the source has likely experienced a past accretion burst, i.e., it is a post-burst source (Lee 2007; Jørgensen et al. 2013). After the burst, the refreeze-out of CO and H_2O should start from the inner high-density region such that the observed peak radii are likely static (Lee 2007; Visser et al. 2015; Hsieh et al. 2018). Therefore, comparing these peak radii with the model, we can estimate the peak luminosity in the past, i.e., the burst luminosity (L_{burst}; Table 3), and identify the post-burst sources with $L_{burst} > L_{bol}$. However, this estimated luminosity is degenerate with the inclination angle for the case of HCO^+ at small scales (Figure 6). This degeneracy becomes severe near the pole-on case (see Appendix B). Fortunately, most of
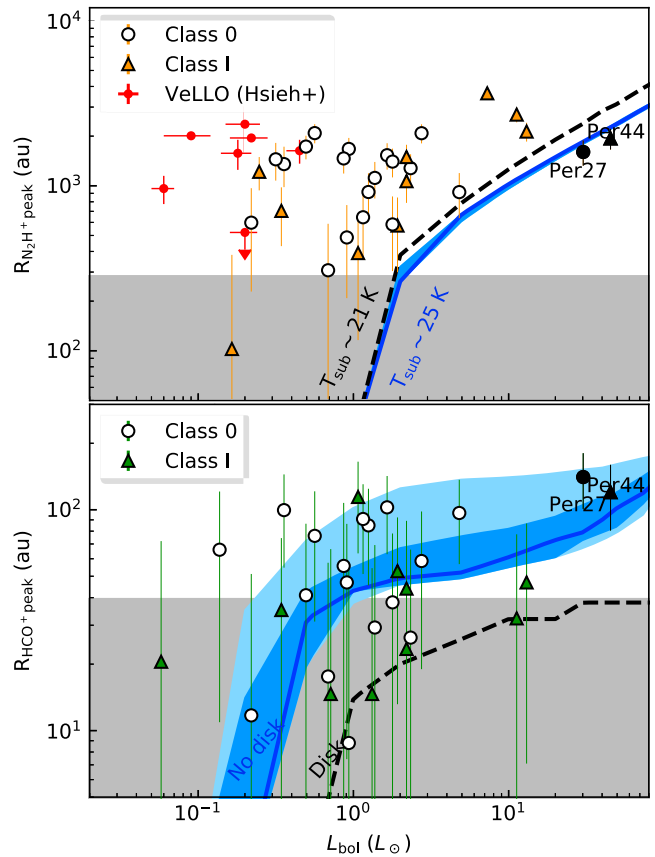
Figure 6. Measured N_2H^+ (top) and HCO^+ peak radii (bottom) as a function of the bolometric luminosities of the sources. The peak positions measured in this work are shown by open circles (Class 0) and filled triangles (Class I), and those from Hsieh et al. (2018) are in red. Per-emb-27 and 44 have been classified as sources undergoing an accretion burst and are plotted in black. We note that the peak position in Hsieh et al. (2018) is measured using abundance profiles, which could result in a slightly higher value. The modeled peak radius as a function of luminosity is shown with the blue lines for an inclination angle $\theta_{inc} = 45°$. The dark-blue and light-blue areas represent a range of $\theta_{inc} = 25°$–$65°$ and $\theta_{inc} = 15°$–$75°$, respectively, for which the upper boundary has a smaller inclination angle ($0°$ for pole-on). The dashed black line shows a model at an inclination angle of $45°$ with a CO sublimation temperature of 21 K (top) and with the presence of a disk (bottom). The gray area corresponds to a half-beam size, the limitation to resolve the depletion in the observations.

our targets show clear bipolar outflows (Stephens et al. 2018), suggesting that they are not pole-on sources. Statistically, the nearly pole-on probability ($\theta_{inc} < 25°$) is less than 10%. Thus, we derive the burst luminosity by comparing the measured peak radius to the model at an inclination angle of $45°$ and use the angle from $25°$ to $75°$ as the uncertainty (Table 3).

As a result, we found that with N_2H^+ almost all Class 0 and Class I sources are identified as post-burst sources. With HCO^+, 10/17 Class 0 sources and 2/10 Class I sources are identified as post-burst sources. The sources with a peak radius less than the half-beam size are not classified as post-burst sources; they are classified as sources without a past burst or sources where CO or H_2O have refrozen onto the dust grains after the last burst.

It is noteworthy that Per-emb-4 has no detection of HCO^+ or CO isotopologues (Hsieh et al. 2018) in the N_2H^+ depletion region. Thus, we are not able to exclude the possibility that the N_2H^+ depletion comes from freeze-out of its parent molecule, N_2.

4.4. Caveat in Identification of the Post-burst Sources

4.4.1. Effect of Optical Depth for Probing the H_2O Snowline

The optical depth from the continuum or line emission could affect the measured peak positions. If the line emission and dust continuum emission are optically thin, the integrated intensity maps should properly reflect the snowline locations. N_2H^+ is expected to be less affected by this issue because it is usually optically thin throughout the outer envelope owing to its relatively low abundance. However, for the H_2O snowline traced by HCO^+ in the inner dense region, the effects of optical depth need to be addressed. Here we discuss how it influences the measured snowline radii in two cases, optically thick HCO^+ line emission and optically thick dust continuum emission:

(a) If the HCO^+ emission is optically thick, it prevents us from probing the inner dense region. An HCO^+ hole would be seen in the HCO^+ integrated intensity map owing to line self-absorption and/or continuum subtraction. In order to reduce this effect, we integrated the spectra avoiding the optically thick regions near the systemic velocity (Table 2; see also Appendix A). Excluding the low-velocity channels should not affect the measured snowline location because it is expected to locate at the inner region where the velocity is high. However, it is unclear what fraction of the continuum emission is absorbed by the foreground HCO^+ gas at the selected velocity ranges for integration, resulting in an "oversubtraction" in the continuum subtraction process. This issue leads to a misidentification of HCO^+ depletion, e.g., as for the case of Per-emb-49 in Figure 9. The current data cannot completely rule out this possibility except for sources with CH_3OH detections (see below).

(b) If the dust continuum emission is optically thick at the frequency of interest, no line emission can escape from such a region. In this case, the HCO^+ line emission will mimic the depletion signature owing to the presence of the water snowline. It is noteworthy that the dust opacity could be increased inside the H_2O snowline because the evaporation of icy grains leads to effective destructive collisions and higher dust densities (Banzatti et al. 2015; Cieza et al. 2016). If this is the case, the HCO^+ depletion toward the center may still reflect the H_2O snowline locations assuming that the optically thick dust region and an associated HCO^+ depleted region are due to a dust opacity change within the water snowline.

Since CH_3OH has a sublimation temperature similar to that of H_2O ($\sim$100 K), CH_3OH line emission can be used as a proxy for the location of the H_2O snowline. For those sources with CH_3OH detections, the measured HCO^+ peak radii broadly agree with the CH_3OH emission extents (Figure 3), which can resolve the issues of optical depths mentioned above. This indicates that the estimates of the H_2O snowline locations from HCO^+ are reasonable at least for these six sources. Thus, we speculate that HCO^+ is a good tracer of the H_2O snowline, but future observations with a resolution sufficient to resolve the continuum source or more warm-gas tracers are required to completely rule out the optical depth issue.

4.4.2. Dependence of the Physical and Chemical Models

The binding energy used in the chemical model determines the sublimation temperature, the decisive parameter for the snowline locations (Collings et al. 2003). The binding energy of pure CO is found between $\sim$850 and 1000 K (Bisschop et al. 2006) but can be increased to $\sim$1200–1700 K depending on the substrate (Fayolle et al. 2016), resulting in a CO sublimation temperature of $\sim$17–33 K at a gas density of $\sim10^7$ cm^{-3}. To make a model that fits the two burst sources (Section 5.1), Per-emb-27 and Per-emb-44, we use binding energies of 1307 K for CO (Noble et al. 2012, measured from amorphous water ice) and 4820 K for H_2O (Sandford & Allamondola 1993; Fraser et al. 2001). Figure 6 shows the modeled curve with the CO binding energy of 1150 K (Collings et al. 2004; $T_{sub} \sim$ 21 K) and 1307 K ($T_{sub} \sim$ 25 K). However, the binding energy is degenerate with the density structures (see below), and the latter are not necessarily the same in different sources.

Although a massive unstable disk is presumed to trigger the accretion burst, we perform our analysis using models without a disk. A protostellar disk can shield the envelope or itself from the central radiation, changing the temperature structure mainly along the equatorial plane (Murillo et al. 2015). Figure 6 (bottom) shows the modeled curve from a disk model in comparison with the no-disk model that is used for the HCO^+ peak radii. A higher central luminosity is required to heat the envelope and shift the H_2O snowline outward for the disk model compared with the no-disk model. If a massive disk is included in the model, the number of post-burst sources and the burst luminosities are expected to increase. However, a disk model is much more complicated since the disk density, geometry, and grain size distribution all affect the temperature structure. To keep the model simple, we chose to use the no-disk model. The no-disk model could be considered as a conservative approach for identifying the occurrence of a past burst. Specifically, the modeled snowline radii are an upper limit, and correspondingly the estimated burst luminosities, L_{burst,H_2O} and $L_{burst,CO}$, are lower limits. MHW20 will provide more details on how the disk size, geometry, envelope density, and other parameters affect the temperature structures and snowline locations.

5. Discussion

5.1. Sources in the Burst Phase

Our sample includes two sources, Per-emb-27 (NGC 1333 IRAS 2A) and Per-emb-44 (SVS 13A), which are likely undergoing an accretion burst given the current huge $L_{bol} = 30\,L_\odot$ and $L_{bol} = 45\,L_\odot$, respectively.

Several complex organic molecules are detected toward Per-emb-27 in the inner 40–100 au region, where the dust temperature is >100 K (Maret et al. 2014; Maury et al. 2014; Taquet et al. 2015). Codella et al. (2014) found a knotty jet driven by Per-emb-27 with a dynamical time of <30–90 yr, which is considered to be a signature of episodic accretion (Vorobyov et al. 2018). Per-emb-44 contains also a central hot region with a detection of glycolaldehyde (De Simone et al. 2017; Bianchi et al. 2019). Multiple components are found in continuum observations by Tobin et al. (2016, 2018), including a close binary with a separation of 0."3 (70 au). Furthermore, Lefèvre et al. (2017) speculate on the existence of a companion with a separation of 20–30 au in order to explain the knotty jets with a period of $\sim$300 yr, a putative companion that triggers the

burst episodes in the close perihelion approach with an eccentric orbit. These results suggest that Per-emb-27 and 44 are in the accretion burst phase.

These burst-phase sources can be used as calibrators for the model. If we assume that the current bolometric luminosity determines the observed CO and H_2O peak radii, the modeled curve in Figure 6 should go through the data points of Per-emb-27 and 44. As a result, the adopted model without a disk component and a CO sublimation temperature of $\sim$25 K looks reasonable (see Section 4.4.2). However, the assumption is not necessarily true because the luminosity variation during a burst can be very large (Elbakyan et al. 2016; Vorobyov et al. 2018). Furthermore, the density structures should be quite different for each source. Thus, this calibration provides only a rough confirmation.

5.2. Chronology of Episodic Accretion in Protostars

In this section we discuss the history of the episodic accretion process in a statistical way from Class 0 to Class I. We derive frequencies of accretion bursts in Section 5.2.1 and mass accretion rates during burst phases in Section 5.2.2. Then, based on these results, we discuss the mass accumulation history of protostars in episodic accretion in Section 5.2.3.

5.2.1. Evolution of Burst Frequency

Estimation of the outburst frequency has been done by monitoring a sample of protostars in the more evolved Class II stage (Scholz et al. 2013; Contreras Peña et al. 2019). These studies require a large survey with a long baseline in time (Hillenbrand & Findeisen 2015). The chemical probes extend the baseline to 1000–10,000 yr by considering the refreeze-out timescales.

The refreeze-out timescales of CO and H_2O are different because their snowlines are located at different radii with different densities. Thus, these two chemical tracers provide complementary information to constrain the time since a past burst. The refreeze-out timescales can be expressed as a function of gas density (n_{H_2}) and dust temperature (T_{dust}), i.e.,

$$\tau_{fr} = 1 \times 10^4 \, yr \sqrt{\frac{10 \, K}{T_{dust}}} \frac{10^6 \, cm^{-3}}{n_{H_2}} \qquad (1)$$

from Visser & Bergin (2012) and Visser et al. (2015). Here we assume that τ_{fr} is 10,000 yr for CO and 1000 yr for H_2O (Visser et al. 2015). As a result, we categorize these targets into the following: (1) post-burst source from HCO^+, where the burst has occurred in the past 1000 yr; (2) post-burst source from N_2H^+ but not from HCO^+, where the burst has occurred during the past 1000–10,000 yr; and (3) no signature from both N_2H^+ and HCO^+. No burst has occurred during the past 10,000 yr (Table 3). Figure 4 shows the intensity profiles of the standard cases for these three categories together with that during an outburst. Table 3 lists the time since the last burst for each source.

Figure 7 shows L_{burst}/L_{bol} as a function of the evolutionary indicator, bolometric temperature (T_{bol}), from both CO and H_2O. Sources with $L_{burst} > L_{bol}$ are identified as post-burst sources, namely, that the source has experienced a past burst within the refreeze-out time. Excluding the two sources in the burst phase (Per-emb-27 and 44, Section 5.1), there are 28 and 27 sources for the following statistical analyses with N_2H^+ and
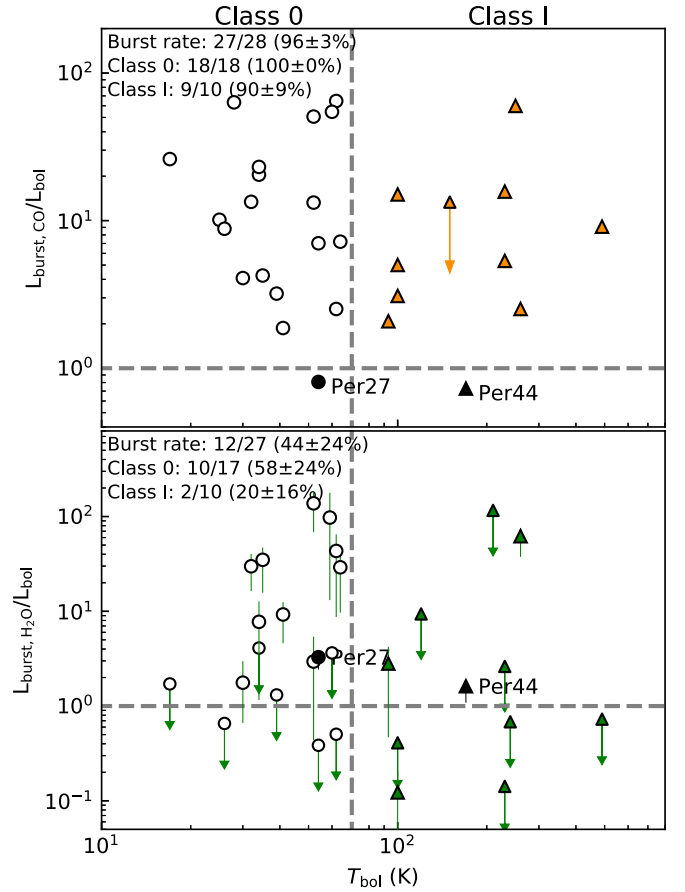
Figure 7. L_{burst}/L_{bol} as a function of the bolometric temperature T_{bol} from N_2H^+ (top, $L_{burst,CO}/L_{bol}$) and HCO^+ (bottom, $L_{burst,H_2O}/L_{bol}$). The markers shown in this plot are the same as those in Figure 6 for Class 0 and Class I sources. The vertical dashed lines indicate the bolometric temperature of 70 K, the boundary between Class 0 and Class I. The horizontal dashed lines represent $L_{burst} > L_{bol}$ for classification of post-burst sources.

HCO^+, respectively. L_{burst} is defined as an upper limit for those sources whose measured peak radius is less than the half-beam size, and the upper limit is obtained using the half-beam size as the peak radius. As a result, we cannot identify the chemical signature of a past burst for Per-emb-51 on the basis of its N_2H^+ map, and for seven sources on the basis of their HCO^+ maps. For Per-emb-51 with N_2H^+, the upper limit of $L_{burst,CO}$, $2.2 \, L_\odot$, suggests that it unlikely experienced a past burst, or at least a strong burst. For those seven sources from L_{burst,H_2O}, depending on the weighting of the map, the upper limits of L_{burst,H_2O} are $0.9 \, L_\odot$ for three sources, $1.8 \, L_\odot$ for two sources, and $6.7 \, L_\odot$ for two sources. These upper limits are generally smaller than the burst luminosities of the post-burst sources, with a median of $31.1 \, L_\odot$ and a standard deviation of $20.8 \, L_\odot$ (Figure 8). Therefore, we do not consider these sources to be post-burst sources. As a result, we find that $100\% \pm 0\%$ of Class 0 objects are post-burst sources and $90\% \pm 9\%$ of Class I objects are post-burst sources from N_2H^+ alone, where the uncertainty is derived using binomial statistics. This result implies that the burst interval is $<10,000$ yr for Class 0 objects and $\sim$11,000 yr $\left(\frac{10,000}{0.9} \, yr\right)$ for Class I objects. From HCO^+ alone, we identify that $58\% \pm 24\%$ of Class 0 objects and $20\% \pm 16\%$ of Class I objects are post-burst sources. This gives us burst intervals of $\sim$1700 yr for Class 0 objects and $\sim$5000 yr for Class I objects. The combination of these results
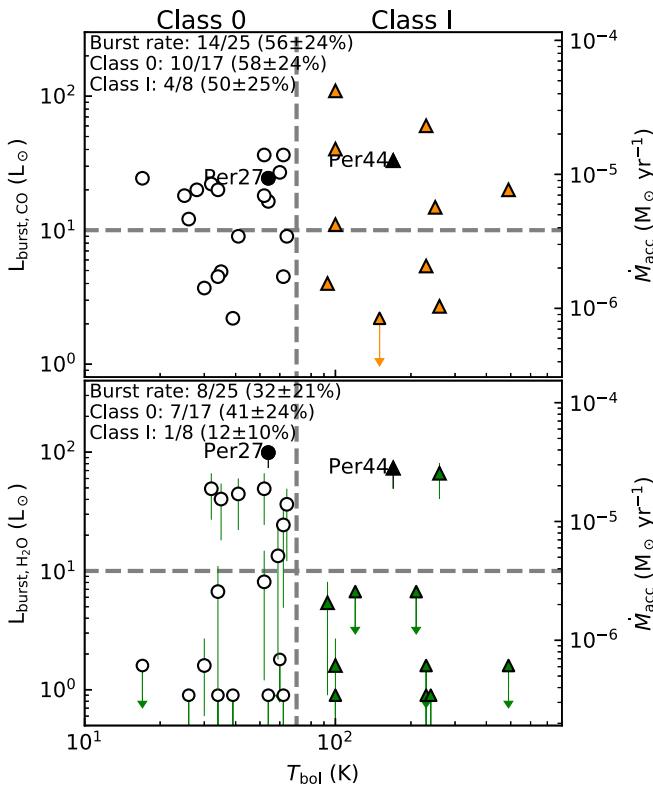
Figure 8. Luminosity during the past burst obtained from N_2H^+ (top) and HCO^+ (bottom) as a function of bolometric temperature. The luminosity is derived by modeling the emission-line peak offset, and sources with an offset less than the half-beam are labeled with the half-beam as an upper limit. The horizontal dashed lines indicate the burst luminosity $L_{burst} > 10 \, L_\odot$. The right axis shows the mass accretion rate derived assuming that the luminosity is dominated by accretion luminosity.

suggests that the burst frequency is decreasing from the Class 0 to the Class I stage.

The criterion used to define post-burst sources, $L_{burst} > L_{bol}$, may not well portray sources during an accretion burst, especially for the estimate of burst frequencies; intuitively, large bursts occur rarely compared with small bursts. For example, several post-burst sources (Per-emb-3, 9, 30, etc.) have their $L_{burst,CO}$ of ~ 2.2–$4.5 \, L_\odot$, only ~ 3–4 times larger than their L_{bol}. These sources may have experienced a small accretion outburst ($\dot{M}_{acc} \sim (1-2) \times 10^{-6} \, M_\odot \, yr^{-1}$; see Section 5.2.2) that is expected to occur more frequently. In addition, the observed bolometric luminosity can be affected by the viewing angle of a disk-outflow system. A small L_{bol} may result from a nearly edge-on configuration (Offner et al. 2012). This can lead to a misidentification of a post-burst source if L_{bol} is very small and if L_{burst} is only slightly larger. Thus, we decide to focus on those post-burst sources robustly identified. If we consider only large outbursts with $L_{burst} > L_{bol}$ and $L_{burst} > 10 \, L_\odot$ (Enoch et al. 2009), $56\% \pm 24\%$ of Class 0 objects and $50\% \pm 25\%$ of Class I objects are post-burst sources from N_2H^+, implying an interval of $\sim 18{,}000$ and $\sim 20{,}000$ yr for Class 0 and Class I, respectively (Figure 8). From HCO^+, there are $41\% \pm 24\%$ of post-burst sources in Class 0 with an interval of ~ 2400 yr and $12\% \pm 10\%$ of post-burst sources in Class I with an interval of ~ 8000 yr (note that two sources with $L_{bol} > 10 \, L_\odot$ are excluded given the new criterion). The inconsistencies between the burst intervals traced with N_2H^+ and HCO^+ are difficult to explain, but this

result still suggests a decrease of burst frequency from the Class 0 stage to the Class I stage. However, from an evolutionary point of view, if a disk is significantly denser/larger at the Class I stage than that at the Class 0 stage, it might shrink the emission peak inward (Figure 6). The disk evolution may thus lead us to underestimate the number of post-burst sources at the Class I stage, and our conclusion that the burst frequency decreases from the Class 0 to the Class I stage might, in turn, not be robust.

Based on N_2H^+ observations, Hsieh et al. (2018) found that episodic accretion can start at a very early evolutionary stage. Here we find that the burst frequency is higher in the Class 0 stage than in the Class I stage. The accretion outbursts are believed to be associated with a massive and large disk with gravitational and/or magnetorotational instability (Zhu et al. 2010a; Vorobyov & Basu 2015). Therefore, the burst frequency may reflect the disk formation and/or evolution. The onset of disk formation is still unclear, but disks have been found in some Class 0 sources (Tobin et al. 2012; Murillo & Lai 2013; Ohashi et al. 2014; Aso et al. 2017; Lee et al. 2017, 2018; Hsieh et al. 2019; Maury et al. 2019). Besides, numerical simulations suggest that an initially unstable cloud core can promote disk formation and tends to have a higher mass accretion rate (Machida et al. 2016). Vorobyov et al. (2013) further support that the episodic accretion process is highly dependent on the core initial conditions; with a higher ratio of rotational to gravitational energy, the strength of the burst is increased.

If accretion bursts are triggered by infalling fragments in a gravitationally unstable disk (Vorobyov & Basu 2005), the decreasing burst frequency implies that, at an earlier stage, either disk fragmentation occurs more frequently or the fragments tend to fall more often onto the central source. It is also noteworthy that Regály & Vorobyov (2017) find that the gravitational instability in Vorobyov & Basu (2005) is overestimated with a fixed central source because the disk angular momentum can translate into the orbital motion of the central source. The gravitational instability can be controlled by infall onto the disk and its thermodynamics (Kratter & Lodato 2016). A high-mass infall rate is crucial for sustaining the gravitational instability in disks (Vorobyov & Basu 2005; Kratter et al. 2008), which might explain the high burst frequency in the Class 0 stage. In addition, fragmentation is suggested to occur in cold regions that require a sufficient cooling time (Kratter et al. 2010; Kratter & Murray-Clay 2011; Vorobyov & Basu 2010). Observations of multiple systems (Murillo et al. 2016; Tobin et al. 2018) in the cold disk/envelope support such fragmentations at an early stage.

5.2.2. Mass Accretion Rate

The derived burst luminosities give us indications on the mass accretion rate during the past burst phase. If we assume that $L_{burst} = L_{acc}$, the accretion luminosity, we derive the mass accretion rate with

$$L_{acc} = \frac{GM_{star}\dot{M}_{acc}}{R}, \qquad (2)$$

where G is the gravitational constant, R is the protostar radius (assumed to be 3 $R_\odot$; Dunham et al. 2010), and M_{star} is the mass of the central source (assumed to be 0.25 $M_\odot$, half of the average stellar mass; Evans et al. 2009). Figure 8 shows

the inferred burst-phase mass accretion rate as a function of the evolutionary indicator $T_{\rm bol}$. This figure aims to reveal the evolution of episodic accretion, while the ratios of the post-burst sources ($> 10 L_\odot$) indicate the burst frequency, and $\dot{M}_{\rm acc}$ represents their burst strength. We find mass accretion rates during the burst phase ($L_{\rm burst} > L_{\rm bol}$ and $L_{\rm burst} > 10 L_\odot$) between $4.2 \times 10^{-6} M_\odot \, {\rm yr}^{-1}$ and $4.2 \times 10^{-5} M_\odot \, {\rm yr}^{-1}$ from N_2H^+ and between $5.1 \times 10^{-6} M_\odot \, {\rm yr}^{-1}$ and $2.5 \times 10^{-5} M_\odot \, {\rm yr}^{-1}$ from HCO^+ (Table 3). The median is $\sim 7.6 \times 10^{-6} M_\odot \, {\rm yr}^{-1}$ from N_2H^+ and $\sim 1.6 \times 10^{-5} M_\odot \, {\rm yr}^{-1}$ from HCO^+ with a standard deviation of $\sim (5.8 - 8.8) \times 10^{-6} M_\odot \, {\rm yr}^{-1}$. This systematic shift might come from the adopted model parameters such as the CO binding energy. From an evolutionary point of view, the median does not change from Class 0 to Class I from both N_2H^+ and HCO^+. However, the estimation has a strong bias in selection, as the analyses only identify those sources with strong bursts. Besides, the assumption of $M_{\rm star} = 0.25 M_\odot$ can be unrealistic, as the stellar mass must increase from the Class 0 to the Class I stage. Thus, $M_{\rm star}$ should be an increasing value as a function of time, and given the similar accretion luminosity during outbursts from Class 0 to Class I, $\dot{M}_{\rm acc}$ is subsequently expected to decrease with time.

5.2.3. Mass Accumulation of Protostars

We have derived the mass accretion rates and the intervals between accretion episodes, which allows us to probe the growing process of the central stars. Considering a lifetime of 0.15–0.24 Myr (Dunham et al. 2015) and an interval of 2400 yr for the Class 0 stage, accretion bursts would occur 63–100 times during this stage. Similarly in Class I, with a lifetime of 0.31–0.48 Myr and an interval of 8000 yr, accretion bursts would occur 39–60 times; note that our sample includes only one late Class I protostar (Per-emb-63) with $T_{\rm bol} > 300 \, {\rm K}$ (Evans et al. 2009), and the burst frequency likely keeps decreasing in the Class I stage; thus, the total burst number might be overestimated in Class I. Besides, if the lifetimes of Class 0 and Class I are 30% shorter as suggested by Carney et al. (2016), the total number of bursts would be revised downward by 30%.

Statistically, Enoch et al. (2009) found that $\sim 5\%$ of the embedded protostars have a high luminosity with $L_{\rm bol} > 10 L_\odot$, or $\dot{M}_{\rm acc} > 10^{-5} M_\odot \, {\rm yr}^{-1}$. If these sources are during the burst phase, each burst would last for $2400 \times 0.05 = 120 \, {\rm yr}$ at the Class 0 stage, which is consistent with the duration of 100–200 yr predicted from simulations of Vorobyov & Basu (2005). Given the median burst-phase accretion rate of $(7.6 - 16.2) \times 10^{-6} M_\odot \, {\rm yr}^{-1}$, each burst would thus deliver $\sim (9.1 - 19.4) \times 10^{-4} M_\odot$ onto the central star. Thus, the protostar would accumulate $\sim 0.06 - 0.19 M_\odot$ at the Class 0 stage and $\sim 0.04 - 0.12 M_\odot$ at the Class I stage. Assuming a mean stellar mass of $0.5 M_\odot$ (Evans et al. 2009), this result implies that only $\sim 20\% - 60\%$ ($0.1 - 0.3 M_\odot$) of mass is accumulated during burst phases. A simple explanation for the discrepancy is that the final stellar mass is in fact smaller; for example, the peak of the initial mass function is $\sim 0.3 M_\odot$ (Muench et al. 2002; Alves et al. 2007). Alternatively, we propose three possibilities to complement the remaining mass accumulated: (1) An underestimation of the burst-phase mass accretion rate. The accretion rate is estimated considering a

model without a disk component such that the derived accretion luminosity is likely a lower limit. (2) Non-negligible mass accumulation during the quiescent phase. As our estimated accumulated mass of $0.1 - 0.3 M_\odot$ in the Class 0/I stage arises solely from the accretion burst, it requires $\lesssim 80\%$ ($0.4 M_\odot$) of the mass accreted in quiescent phase with $\dot{M}_{\rm acc} \lesssim (5.6 - 8.7) \times 10^{-7} M_\odot \, {\rm yr}^{-1}$ to build a star with an average mass of $0.5 M_\odot$. (3) The existence of superbursts (i.e., FU ori type). Offner & McKee (2011) estimate that $\sim 25\%$ of mass is accreted during the FU ori events with $\dot{M}_{\rm acc} \sim 10^{-5} - 10^{-4} M_\odot \, {\rm yr}^{-1}$. This is consistent with the highest mass accretion rate estimated from the N_2H^+ observations as $\sim 4.2 \times 10^{-5} M_\odot \, {\rm yr}^{-1}$. If such superbursts last for longer, they could deliver significant material onto the central sources.

6. Summary

We present our ALMA cycle 5 observations of N_2H^+ $(1-0)$ and HCO^+ $(3-2)$ toward 39 Class 0 and Class I sources. We analyze the spatial distributions of these two molecules, and by comparing to our chemical models, we derive the required luminosity that sublimates CO and H_2O and destroys N_2H^+ and HCO^+, respectively. We compare such derived luminosity to the bolometric luminosity (the current luminosity), thus identifying the sources that experienced a past accretion burst with $L_{\rm burst} > L_{\rm bol}$, i.e., the post-burst sources. Our results are summarized as follows:

1. N_2H^+ and HCO^+ peak positions can be used to trace the CO and H_2O sublimation regions, respectively, and in turn to estimate the luminosity during the past burst. While N_2H^+ at large scale is less affected by the system geometry, HCO^+ in the inner regions is sensitive to the inclination angle but is crucial to trace the past burst over a shorter timescale.

2. We find that 7/17 Class 0 and 1/8 Class I are post-burst sources from HCO^+. This decrease of the fraction of post-burst sources may result from the evolution of burst frequency, but we cannot exclude the possibility that the snowline radius is shrunk owing to the increase of disk density/size from the Class 0 to the Class I stage. If the disk evolution is not the main factor, then we can draw the following conclusions about the mass accumulation history from the Class 0 to the Class I stage.

3. We derive the intervals between accretion episodes of ~ 2400 yr for Class 0 sources and ~ 8000 yr for Class I sources, suggestive of a decrease in burst frequency during the embedded phase. If the accretion outburst is triggered by disk fragmentation due to gravitational instability, our result suggests that the fragmentation occurs more frequently at an earlier evolutionary stage. Alternatively, the fragment has a higher probability to fall onto the central star at such a stage.

4. We estimate the mass accretion rates at the burst phase to be $(7.6-16.2) \times 10^{-6} M_\odot \, {\rm yr}^{-1}$. From an evolutionary point of view, the burst magnitude is likely unchanged from Class 0 to Class I.

5. Based on the estimate of mass accretion rate and interval between episodes, we derive an accumulated mass of $0.06 - 0.19 M_\odot$ at the Class 0 stage and $\sim 0.04 - 0.12 M_\odot$ at the Class I stage, in total $0.1 - 0.3 M_\odot$ during burst phases. This value is smaller than the typical stellar mass of

0.3–0.5 $M_\odot$. More material needs to be accreted to build the star during the quiescent phase, or perhaps the star can accumulate mass via a few super accretion bursts.

Appendix A
Comparison of Continuum-subtracted HCO$^+$ Maps

Figure 9 shows the HCO$^+$ integrated intensity maps toward the 39 targets. The selected velocity ranges for integration are listed in Table 2. To study the influences from these selections, Figure 10 shows the images of five selected targets with four types of maps for comparison: (1) normal integration without continuum subtraction, (2) normal integration with continuum subtraction, (3) integration in the optically thin region without continuum subtraction, and (4) integration in the optically thin region with continuum subtraction. The emission peaks in the type 1 maps are mostly toward the source center. However, with continuum subtraction shown in type 2, a hole appears at the center and three of them have negative values. Such negative values come from the "oversubtraction" for the continuum emission (or strong-line absorption) when a significant fraction of the continuum emission is absorbed by the foreground molecular gas. Thus, this hole does not properly reflect the HCO$^+$ spatial distribution. We therefore integrated the flux, avoiding the optically thick region near the central velocity that is shown in type 3; we integrated the velocity ranges, excluding the central channels in between the peak of the blue- and redshifted emission (Figure 10 and Table 2). As a result, after continuum subtraction, type 4, the negative contours disappear toward the central region. This process still cannot completely remove the oversubtraction because the continuum emission is also absorbed by molecular gas at the selected velocity range. However, the fraction of the absorbed continuum emission should not be significant if the selected velocity range is optically thin. Thus, this process likely minimizes the issue of oversubtraction.

HCO$^+$ (3 − 2)
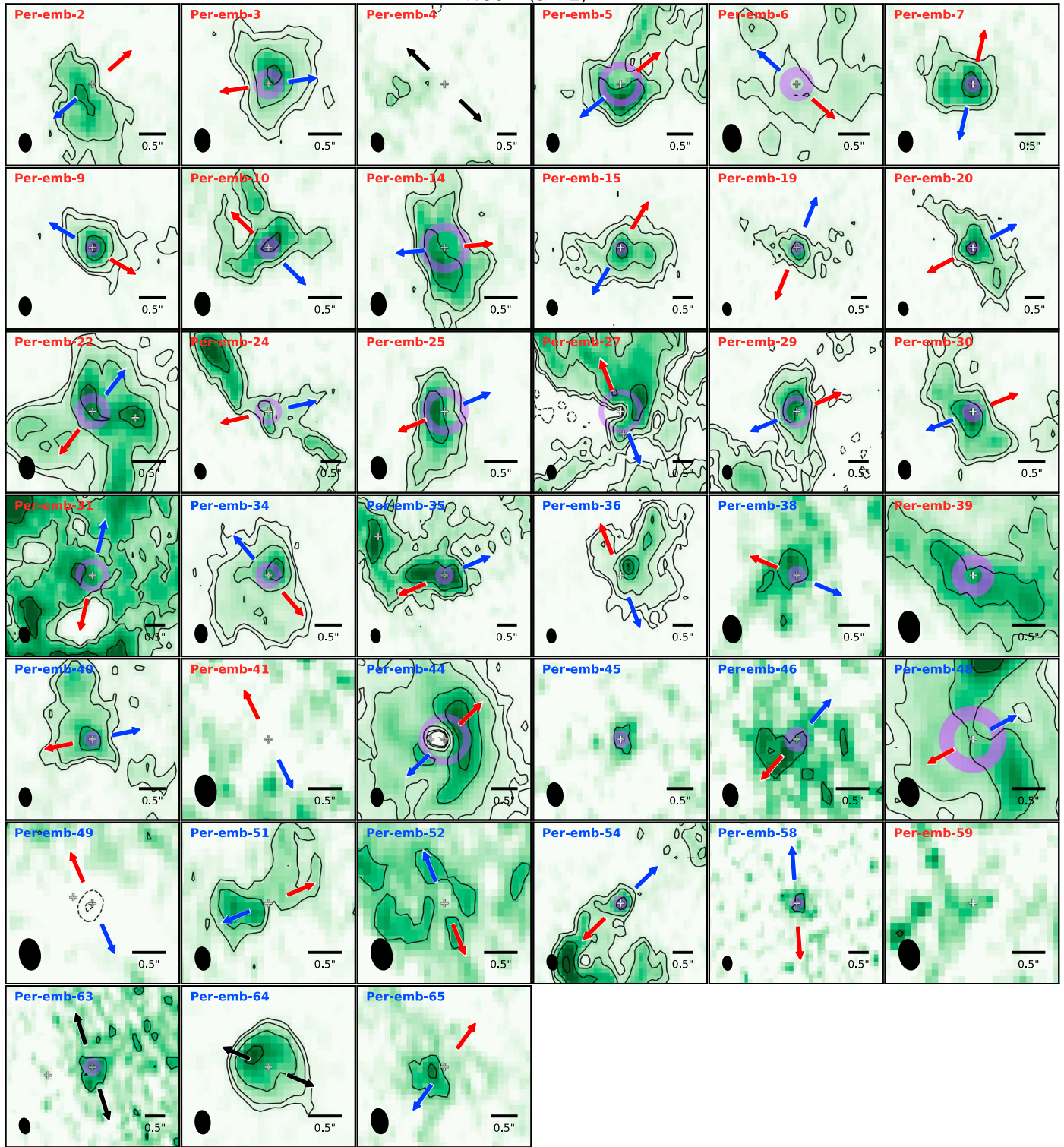
Figure 9. Same as Figure 2, but for HCO$^+$ integrated intensity maps. The contour levels are 3σ, 5σ, 10σ, 20σ, 30σ, and 40σ, with σ the rms noise level given in Table 2. The black bar in the lower right corner indicates a size of 0.″5, while the size of the image is adjusted panel by panel. The purple circles represent the radii of the measured HCO$^+$ peak, with the thickness representing the uncertainties (see the text for detail).
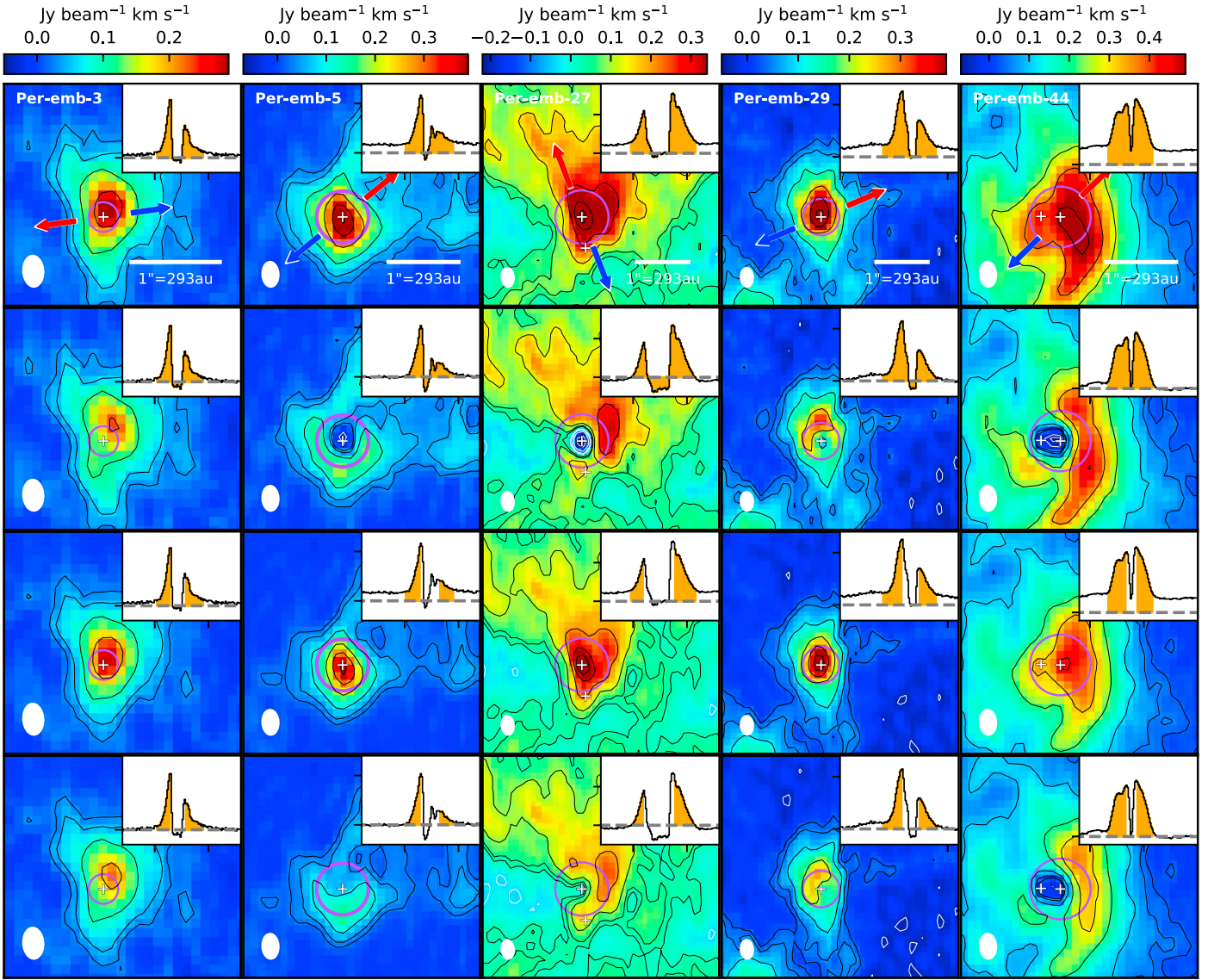
Figure 10. Comparison of HCO$^+$ integrated intensity maps with different velocity ranges with and without continuum subtraction. The panels from top to the bottom are (1) normal integration without continuum subtraction, (2) normal integration with continuum subtraction, (3) integration in the optically thin region without continuum subtraction, and (4) integration in the optically thin region with continuum subtraction. The contour levels are $\pm3\sigma$, $\pm5\sigma$, $\pm10\sigma$, $\pm20\sigma$, $\pm30\sigma$, and $\pm40\sigma$; the positive (negative) values are shown in black (white). The insert in each panel shows the spectrum and the integration ranges in orange. The fluxes are on arbitrary scales, and the gray dashed line marks the zero level. The purple circles indicate the radii of the measured peak positions.

Appendix B
Modeled Images and Their Measured Peak Radii

To compare with observations, we make N$_2$H$^+$ and HCO$^+$ images from our chemical models. We assume a Keplerian motion within 100 au around a protostar with a central mass $M_{star} = 0.25\,M_\odot$. At a radius beyond 100 au, the envelope follows the conservation of angular momentum and freefall with a rotation velocity $\propto r^{-1}$ and a radial velocity $\propto r^{-0.5}$. Together with the given temperature, density, and molecular abundance, we use the line radiative transfer code, available in RADMC3D (Dullemond et al. 2012), to produce the images. We make the images with inclination angles of 15°, 25°, 45°, 65°, and 75° and convolve them by a Gaussian with an FWHM of 1″93 for the N$_2$H$^+$ (1−0) maps and 0″27 for the HCO$^+$ (3 −2) maps, about the equivalent width of the observational beams. To demonstrate inclination effects, here we show an example with $L = 30\,L_\odot$ at five inclination angles including the

edge-on and pole-on cases (Figures 11 and 12). Although the inclination angle does not significantly change the peak radius of N$_2$H$^+$, it influences that of HCO$^+$ on small scales. At the nearly pole-on configuration ($\theta_{inc} \lesssim 20°$), the peak of the HCO$^+$ emission is associated with gas at a higher latitude rather than that in the midplane; thus, it is dominated by the large-scale envelope rather than the inner H$_2$O snowline location (Figure 13). In such a case, the HCO$^+$ peak positions are located at a larger radius depending on the outflow opening angle. In addition, toward larger inclination angles, the redshifted component from the rotating inner envelope can be absorbed by foreground infalling core such that only the blueshifted component is left. This opacity influence is expected to depend on the input density and the input velocity field. We note that the modeled images have negligible dust continuum emission. Thus, the "oversubtraction" issue does not exist, and we integrate the full line profiles (Appendix A). It is also noteworthy that the peak position of the integrated intensity map can change with a
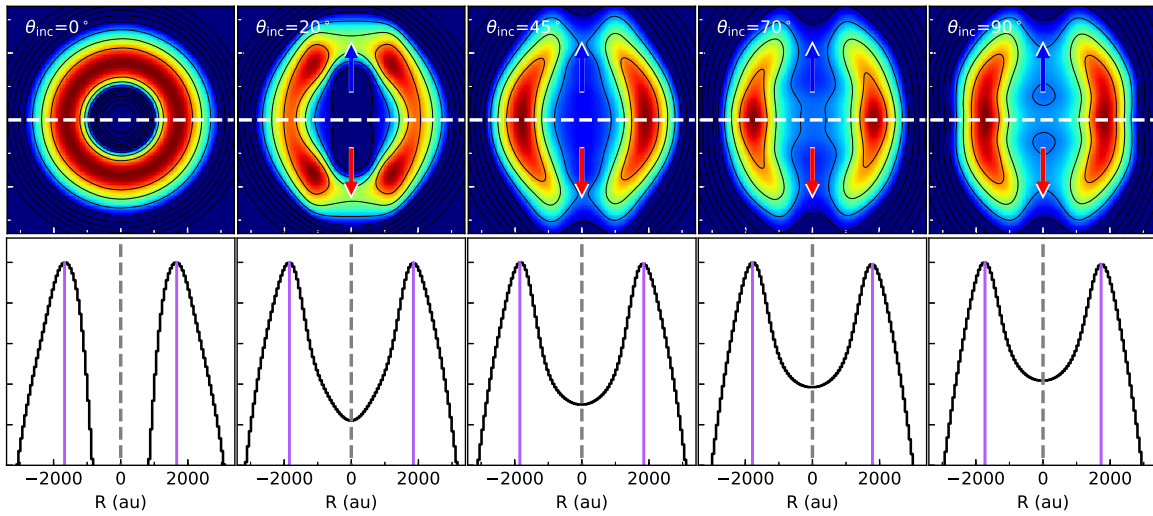
Figure 11. Top: N_2H^+ (1−0) modeled images at different inclination angles (0° for pole-on) for a source with $L = 30\,L_\odot$. The images are normalized to the peak value with a contour step of 10%. The horizontal dashed lines show the cut used for the intensity profile in the bottom panel. Bottom: intensity profiles along a horizontal cut for each modeled image. The x-axis is in the same scale as the above image for comparison. The dashed line represents the source position. The purple vertical lines indicate the measured peak positions that are used to compare with the observed images.
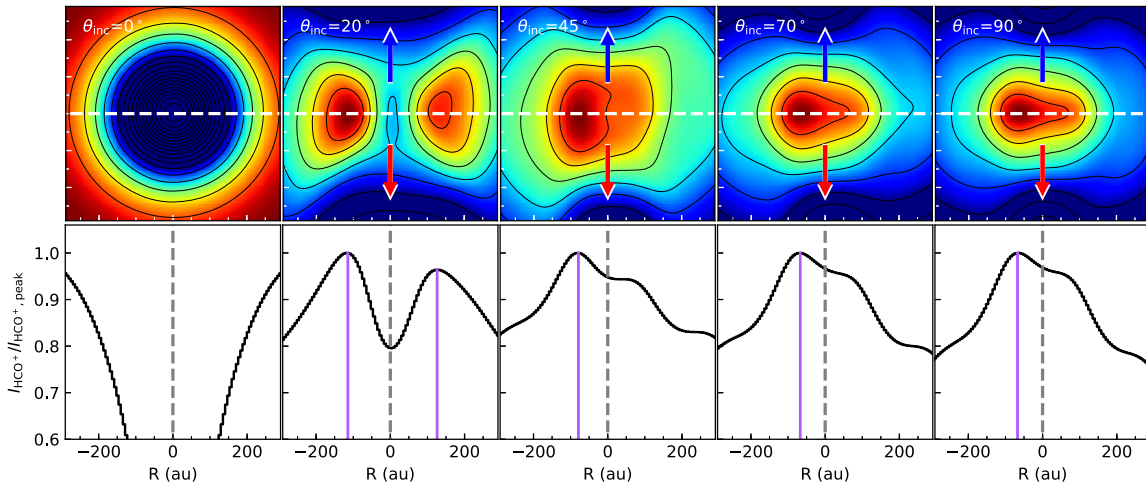
Figure 12. Same as Figure 11, but for HCO^+ (3−2) with a contour step of 5%.
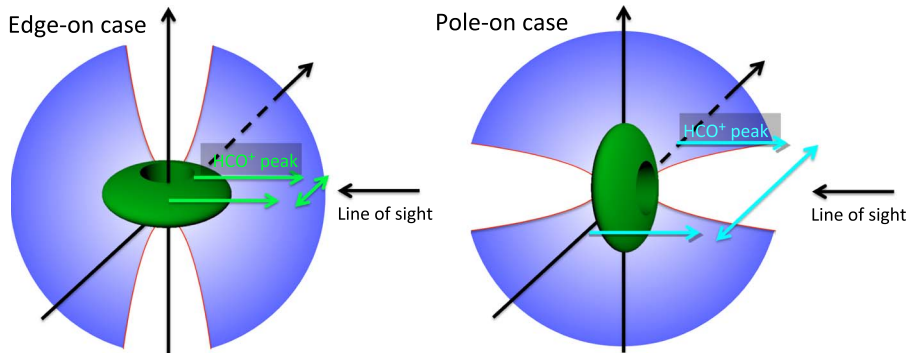
Figure 13. Schematic illustration for the shift of HCO^+ peak positions from the edge-on to pole-on case. This scenario suggests that the HCO^+ emission is dominated by the inner region in the edge-on case and by the outer envelope in the pole-on case.

different selected velocity ranges; the velocity range will decide the emitting regions that contribute to the map depending on the inclination angle. As a result, the modeled curves of emission peak as a function of luminosity are shown in Figure 6 in

comparison with observations. Because of the convolution, a transition close to the half-beam size is shown in Figure 6, denoting the limit of the resolution in our observation for resolving the central depletion.

Appendix C
Intensity Profiles

To check the correlation between the two pairs of molecules, N_2H^+–HCO^+ and HCO^+–CH_3OH, we plot the intensity profiles across the source centers and the measured peaks from Section 4.1 (Figures 14 and 15); CH_3OH is plotted in the only six sources with detections toward the center. Anticorrelation between these pairs of molecules is found in most of the cases, and the measured peak positions are reasonable.
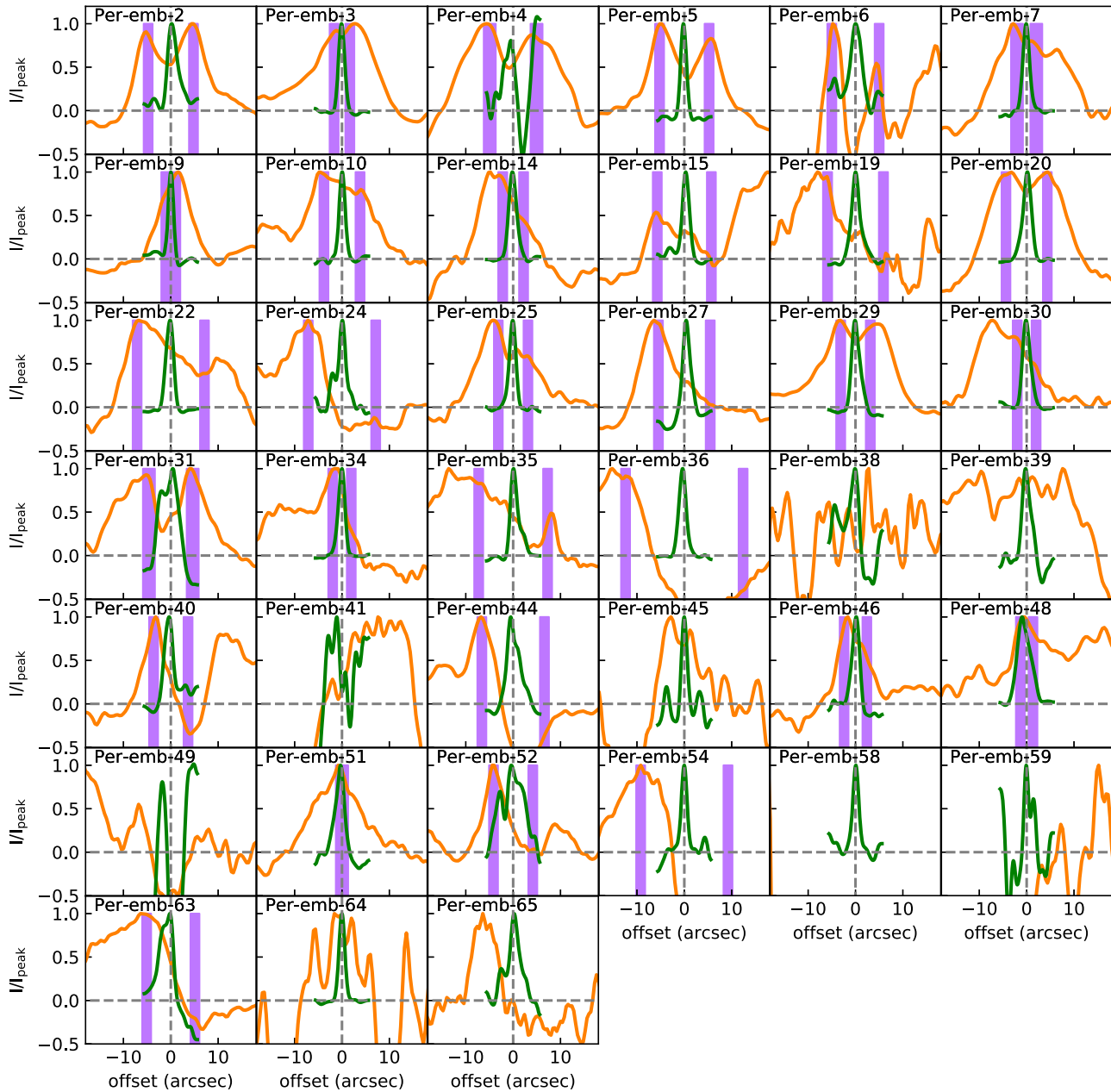
Figure 14. Same as the top panel of Figure 4 (N_2H^+ and HCO^+), but for all of the sources.
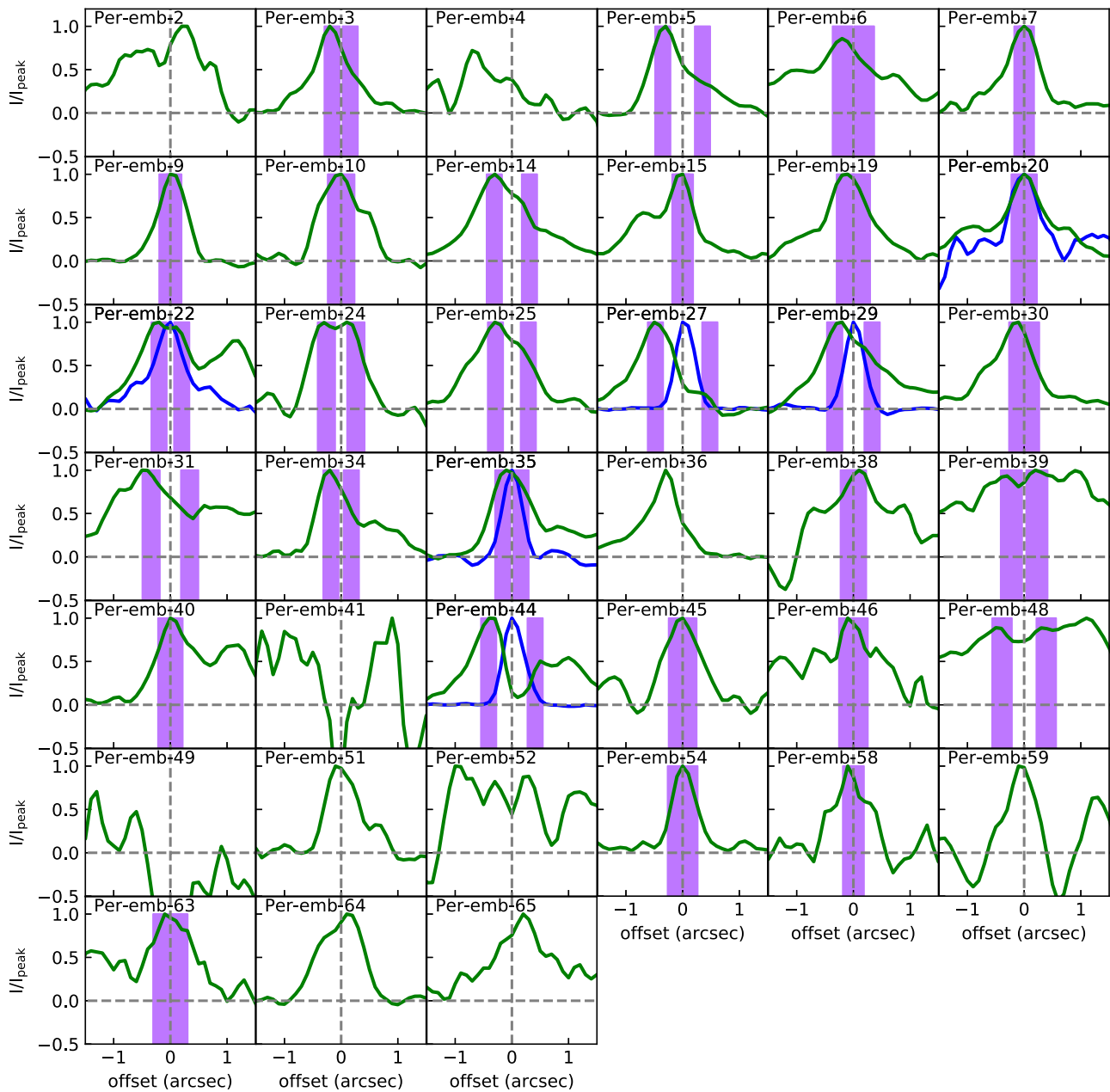
Figure 15. Same as the bottom panel of Figure 4 (HCO$^+$ and CH$_3$OH), but for all of the sources.

ORCID iDs

Tien-Hao Hsieh ⓘ https://orcid.org/0000-0002-5507-5697
Arnaud Belloche ⓘ https://orcid.org/0000-0003-0046-6217
Naomi Hirano ⓘ https://orcid.org/0000-0001-9304-7884
Catherine Walsh ⓘ https://orcid.org/0000-0001-6078-786X
Ewine F. van Dishoeck ⓘ https://orcid.org/0000-0001-7591-1907
Jes K. Jørgensen ⓘ https://orcid.org/0000-0001-9133-8047
Shih-Ping Lai ⓘ https://orcid.org/0000-0001-5522-486X

References

Ábrahám, P., Kóspál, Á., Csizmadia, S., et al. 2004, A&A, 419, L39
Acosta-Pulido, J. A., Kun, M., Ábrahám, P., et al. 2007, AJ, 133, 2020
Alves, J., Lombardi, M., & Lada, C. J. 2007, A&A, 462, L17
Anderl, S., Maret, S., Cabrit, S., et al. 2016, A&A, 591, A3
Andrews, S. M., Rothberg, B., & Simon, T. 2004, ApJL, 610, L45

Armitage, P. J., Livio, M., & Pringle, J. E. 2001, MNRAS, 324, 705
Aso, Y., Ohashi, N., Aikawa, Y., et al. 2017, ApJ, 850, 2
Aspin, C., Reipurth, B., Beck, T. L., et al. 2009, ApJL, 692, L67
Astropy Collaboration, Robitaille, T. P., Tollerud, E. J., et al. 2013, A&A, 558, A33
Audard, M., Ábrahám, P., Dunham, M. M., et al. 2014, in Protostars and Planets VI, ed. H. Beuther et al. (Tucson, AZ: Univ. Arizona Press), 387
Banzatti, A., Pinilla, P., Ricci, L., et al. 2015, ApJL, 815, L15
Bell, K. R., & Lin, D. N. C. 1994, ApJ, 427, 987
Belloche, A., & André, P. 2004, A&A, 418, L35
Bianchi, E., Codella, C., Ceccarelli, C., et al. 2019, MNRAS, 483, 1850
Bisschop, S. E., Fraser, H. J., Öberg, K. I., et al. 2006, A&A, 449, 1297
Bjerkeli, P., Jørgensen, J. K., Bergin, E. A., et al. 2016, A&A, 595, 39
Boley, A. C., & Durisen, R. H. 2008, ApJ, 685, 1193
Caratti o Garatti, A., Garcia Lopez, R., Scholz, A., et al. 2011, A&A, 526, L1
Caratti o Garatti, A., Stecklum, B., Garcia Lopez, R., et al. 2016, NatPh, 13, 276
Carney, M. T., Yıldız, U. A., Mottram, J. C., et al. 2016, A&A, 586, A44
Cieza, L. A., Casassus, S., Tobin, J., et al. 2016, Natur, 535, 258
Clarke, C. J., & Syer, D. 1996, MNRAS, 278, L23

Codella, C., Maury, A. J., Gueth, F., et al. 2014, A&A, 563, L3
Collings, M. P., Anderson, M. A., Chen, R., et al. 2004, MNRAS, 354, 1133
Collings, M. P., Dever, J. W., Fraser, H. J., et al. 2003, ApJ, 583, 1058
Contreras Peña, C., Naylor, T., & Morrell, S. 2019, MNRAS, 486, 4590
Covey, K. R., Hillenbrand, L. A., Miller, A. A., et al. 2011, AJ, 141, 40
Davis, C. J., Scholz, P., Lucas, P., Smith, M. D., & Adamson, A. 2008, MNRAS, 387, 954
De Simone, M., Codella, C., Testi, L., et al. 2017, A&A, 599, A121
Dullemond, C. P., Juhasz, A., Pohl, A., et al. 2012, RADMC-3D: A Multi-purpose Radiative Transfer Tool v0.41, Astrophysics Source Code Library, ascl:1202.015
Dunham, M. M., Allen, L. E., Evans, N. J., II, et al. 2015, ApJS, 220, 11
Dunham, M. M., Evans, N. J., Bourke, T. L., et al. 2010, ApJ, 721, 995
Dunham, M. M., Stutz, A. M., Allen, L. E., et al. 2014, in Protostars and Planets VI, ed. H. Beuther et al. (Tucson, AZ: Univ. Arizona Press), 195
Elbakyan, V. G., Vorobyov, E. I., & Glebova, G. M. 2016, ARep, 60, 879
Enoch, M. L., Evans, N. J., II, Sargent, A. I., & Glenn, J. 2009, ApJ, 692, 973
Evans, N. J., II, Dunham, M. M., Jørgensen, J. K., et al. 2009, ApJS, 181, 321
Fayolle, E. C., Balfe, J., Loomis, R., et al. 2016, ApJL, 816, L28
Fedele, D., van den Ancker, M. E., Petr-Gotzens, M. G., & Rafanelli, P. 2007, A&A, 472, 207
Flower, D. R. 1999, MNRAS, 305, 651
Forgan, D., & Rice, K. 2010, MNRAS, 402, 1349
Fraser, H. J., Collings, M. P., McCoustra, M. R. S., et al. 2001, MNRAS, 327, 1165
Frimann, S., Jørgensen, J. K., Dunham, M. M., et al. 2017, A&A, 602, A120
Gaches, B. A. L., Offner, S. S. R., & Bisbas, T. G. 2019, ApJ, 878, 105
Green, S. 1975, ApJ, 201, 366
Hartmann, L., & Kenyon, S. J. 1996, ARA&A, 34, 207
Herbig, G. H. 1966, VA, 8, 109
Herbig, G. H. 1977, ApJ, 217, 693
Herczeg, G. J., Johnstone, D., Mairs, S., et al. 2017, ApJ, 849, 43
Hillenbrand, L. A., & Findeisen, K. P. 2015, ApJ, 808, 68
Hsieh, T.-H., Hirano, N., Belloche, A., et al. 2019, ApJ, 871, 100
Hsieh, T.-H., & Lai, S.-P. 2013, ApJS, 205, 5
Hsieh, T.-H., Lai, S.-P., & Belloche, A. 2017, AJ, 153, 173
Hsieh, T.-H., Lai, S.-P., Belloche, A., & Wyrowski, F. 2016, ApJ, 826, 68
Hsieh, T.-H., Murillo, N. M., Belloche, A., et al. 2018, ApJ, 854, 15
Johnstone, D., Herczeg, G. J., Mairs, S., et al. 2018, ApJ, 854, 31
Jørgensen, J. K., Schöier, F. L., & van Dishoeck, E. F. 2004, A&A, 416, 603
Jørgensen, J. K., Visser, R., Sakai, N., et al. 2013, ApJL, 779, L22
Jørgensen, J. K., Visser, R., Williams, J. P., & Bergin, E. A. 2015, A&A, 579, A23
Kim, H. J., Evans, N. J., II, Dunham, M. M., et al. 2011, ApJ, 729, 84
Kim, H. J., Evans, N. J., II, Dunham, M. M., Lee, J.-E., & Pontoppidan, K. M. 2012, ApJ, 758, 38
Kóspál, Á., Ábrahám, P., Acosta-Pulido, J. A., et al. 2011, A&A, 527, A133
Kóspál, Á., Ábrahám, P., Prusti, T., et al. 2007, A&A, 470, 211
Kratter, K., & Lodato, G. 2016, ARA&A, 54, 271
Kratter, K. M., Matzner, C. D., & Krumholz, M. R. 2008, ApJ, 681, 375
Kratter, K. M., Matzner, C. D., Krumholz, M. R., et al. 2010, ApJ, 708, 1585
Kratter, K. M., & Murray-Clay, R. A. 2011, ApJ, 740, 1
Krumholz, M. R., Bate, M. R., Arce, H. G., et al. 2014, in Protostars and Planets VI, ed. H. Beuther et al. (Tucson, AZ: Univ. Arizona Press), 243
Kryukova, E., Megeath, S. T., Gutermuth, R. A., et al. 2012, ApJ, 144, 31
Lee, C.-F., Li, Z.-Y., Hirano, N., et al. 2018, ApJ, 863, 94
Lee, C.-F., Li, Z.-Y., Ho, P. T. P., et al. 2017, ApJ, 843, 1
Lee, J.-E. 2007, JKAS, 40, 83
Lee, K. I., Dunham, M. M., Myers, P. C., et al. 2015, ApJ, 814, 114
Lee, K. I., Dunham, M. M., Myers, P. C., et al. 2016, ApJL, 820, L2
Lefèvre, C., Cabrit, S., Maury, A. J., et al. 2017, A&A, 604, L1
Lin, D. N. C., Faulkner, J., & Papaloizou, J. 1985, MNRAS, 212, 105
Liu, H. B., Dunham, M. M., Pascucci, I., et al. 2018, A&A, 612, A54
Liu, H. B., Takami, M., Kudo, T., et al. 2016, SciA, 2, e1500875
Liu, S.-Y., Su, Y.-N., Zinchenko, I., Wang, K.-S., & Wang, Y. 2018, ApJL, 863, L12
Lodato, G., & Clarke, C. J. 2004, MNRAS, 353, 841
Machida, M. N., Inutsuka, S.-I., & Matsumoto, T. 2011, ApJ, 729, 42
Machida, M. N., Matsumoto, T., & Inutsuka, S.-I. 2016, MNRAS, 463, 4246
Maret, S., Belloche, A., Maury, A. J., et al. 2014, A&A, 563, L1
Mauersberger, R., & Henkel, C. 1991, A&A, 245, 457

Maury, A. J., André, P., Testi, L., et al. 2019, A&A, 621, A76
Maury, A. J., Belloche, A., André, P., et al. 2014, A&A, 563, L2
McElroy, D., Walsh, C., Markwick, A. J., et al. 2013, A&A, 550, A36
McMullin, J. P., Waters, B., Schiebel, D., et al. 2007, in ASP Conf. Ser. 376, Astronomical Data Analysis Software and Systems XVI, ed. R. A. Shaw, F. Hill, & D. J. Bell (San Francisco, CA: ASP), 127
Mercer, A., & Stamatellos, D. 2017, MNRAS, 465, 2
Muench, A. A., Lada, E. A., Lada, C. J., et al. 2002, ApJ, 573, 366
Murillo, N. M., Bruderer, S., van Dishoeck, E. F., et al. 2015, A&A, 579, A114
Murillo, N. M., & Lai, S.-P. 2013, ApJL, 764, L15
Murillo, N. M., van Dishoeck, E. F., Tobin, J. J., et al. 2016, A&A, 592, A56
Noble, J. A., Congiu, E., Dulieu, F., & Fraser, H. J. 2012, MNRAS, 421, 768
Offner, S. S. R., Dunham, M. M., Lee, K. I., Arce, H. G., & Fielding, D. B. 2016, ApJL, 827, L11
Offner, S. S. R., Klein, R. I., McKee, C. F., & Krumholz, M. R. 2009, ApJ, 703, 131
Offner, S. S. R., & McKee, C. F. 2011, ApJ, 736, 53
Offner, S. S. R., Robitaille, T. P., Hansen, C. E., et al. 2012, ApJ, 753, 98
Ohashi, N., Saigo, K., Aso, Y., et al. 2014, ApJ, 796, 131
Ortiz-León, G. N., Loinard, L., Dzib, S. A., et al. 2018, ApJ, 865, 73
Padoan, P., Haugbølle, T., & Nordlund, Å 2014, ApJ, 797, 32
Padovani, M., Marcowith, A., Hennebelle, P., et al. 2016, A&A, 590, A8
Plunkett, A. L., Arce, H. G., Corder, S. A., et al. 2013, ApJ, 774, 22
Regály, Z., & Vorobyov, E. 2017, A&A, 601, A24
Riaz, R., Vanaverbeke, S., & Schleicher, D. R. G. 2018, A&A, 614, A53
Ridge, N. A., Francesco, J. D., Kirk, H., et al. 2006, AJ, 131, 2921
Robitaille, T., & Bressert, E. 2012, APLpy: Astronomical Plotting Library in Python v1.1.1, Astrophysics Source Code Library, ascl:1208.017
Robitaille, T. P., Whitney, B. A., Indebetouw, R., et al. 2006, ApJS, 167, 256
Safron, E. J., Fischer, W. J., Megeath, S. T., et al. 2015, ApJL, 800, L5
Sandford, S. A., & Allamandola, L. J. 1993, ApJ, 417, 815
Schnee, S., Sadavoy, S., Di Francesco, J., Johnstone, D., & Wei, L. 2012, ApJ, 755, 178
Schöier, F. L., van der Tak, F. F. S., van Dishoeck, E. F., & Black, J. H. 2005, A&A, 432, 369
Scholz, A., Froebrich, D., & Wood, K. 2013, MNRAS, 430, 2910
Segura-Cox, D. M., Looney, L. W., Tobin, J. J., et al. 2018, ApJ, 866, 161
Stamatellos, D., Whitworth, A. P., & Hubber, D. A. 2011, ApJ, 730, 32
Stamatellos, D., Whitworth, A. P., & Hubber, D. A. 2012, MNRAS, 427, 1182
Stephens, I. W., Dunham, M. M., Myers, P. C., et al. 2018, ApJS, 237, 22
Takami, M., Fu, G., Liu, H. B., et al. 2018, ApJ, 864, 20
Taquet, V., López-Sepulcre, A., Ceccarelli, C., et al. 2015, ApJ, 804, 81
Taquet, V., Wirström, E. S., & Charnley, S. B. 2016, ApJ, 821, 46
Tobin, J. J., Dunham, M. M., Looney, L. W., et al. 2015, ApJ, 798, 61
Tobin, J. J., Hartmann, L., Chiang, H.-F., et al. 2012, Natur, 492, 83
Tobin, J. J., Looney, L. W., Li, Z.-Y., et al. 2016, ApJ, 818, 73
Tobin, J. J., Looney, L. W., Li, Z.-Y., et al. 2018, ApJ, 867, 43
Ulrich, R. K. 1976, ApJ, 210, 377
van 't Hoff, M. L. R., Persson, M. V., Harsono, D., et al. 2018a, A&A, 613, A29
van 't Hoff, M. L. R., Tobin, J. J., Trapman, L., et al. 2018b, ApJL, 864, L23
van 't Hoff, M. L. R., Walsh, C., Kama, M., Facchini, S., & van Dishoeck, E. F. 2017, A&A, 599, A101
Visser, R., & Bergin, E. A. 2012, ApJL, 754, L18
Visser, R., Bergin, E. A., & Jørgensen, J. K. 2015, A&A, 577, A102
Vorobyov, E. I., & Basu, S. 2005, ApJL, 633, L137
Vorobyov, E. I., & Basu, S. 2010, ApJ, 719, 1896
Vorobyov, E. I., & Basu, S. 2015, ApJ, 805, 115
Vorobyov, E. I., DeSouza, A. L., & Basu, S. 2013, ApJ, 768, 131
Vorobyov, E. I., Elbakyan, V. G., Plunkett, A. L., et al. 2018, A&A, 613, A18
Whitney, B. A., Wood, K., Bjorkman, J. E., et al. 2003, ApJ, 598, 1079
Wiebe, D. S., Molyarova, T. S., Akimkin, V. V., Vorobyov, E. I., & Semenov, D. A. 2019, MNRAS, 485, 1843
Yıldız, U. A., Kristensen, L. E., van Dishoeck, E. F., et al. 2012, A&A, 542, A86
Yıldız, U. A., Kristensen, L. E., van Dishoeck, E. F., et al. 2015, A&A, 576, A109
Yoo, H., Lee, J.-E., Mairs, S., et al. 2017, ApJ, 849, 69
Zhu, Z., Hartmann, L., & Gammie, C. 2009, ApJ, 694, 1045
Zhu, Z., Hartmann, L., & Gammie, C. 2010a, ApJ, 713, 1143
Zhu, Z., Hartmann, L., Gammie, C. F., et al. 2010b, ApJ, 713, 1134